Spreading-rate Dependent Mid-ocean Ridge Processes Expressed in Western Atlantic Lithosphere

A Thesis
Presented to
The Academic Faculty

by

Sangmyung David Kim

In Partial Fulfillment
of the Requirements for the Degree
Doctor of Philosophy in the
School of Earth and Atmospheric Sciences

Georgia Institute of Technology
August 2006

Spreading-rate Dependent Mid-ocean Ridge Processes Expressed in Western Atlantic Lithosphere

Approved by:

Dr. Daniel Lizarralde, Advisor
School of Earth and Atmospheric Sciences
Georgia Institute of Technology

Dr. Jean Lynch-Stieglitz
School of Earth and Atmospheric Sciences
Georgia Institute of Technology

Dr. Tim Long
School of Earth and Atmospheric Sciences
Georgia Institute of Technology

Dr. James Gaherty
Lamont-Doherty Earth Observatory
Columbia University

Dr. Robert Lowell
School of Earth and Atmospheric Sciences
Georgia Institute of Technology

Date Approved: May 02, 2006

Ocean is not silent. All my days have I watched it and listened to it, and I know it well. At first it told to me only the plain little tales of calm beaches and near ports, but with the years it grew more friendly and spoke of other things; of things more strange and more distant in space and time.

H. P. Lovecraft, The White Ship

ACKNOWLEDGMENTS

I am deeply indebted to my teachers, colleagues, family members, and friends. I really appreciate my parents for their sincere love and care. I will miss Late Kim Hwang who was my younger brother for the rest of my life. The work presented in this thesis could not have been accomplished without the support and help of Dr. Dan Lizarralde. I thank the captain and crew of the R/V *Maurice Ewing*; C.Hollinshead, R. Milan, and D.Willoughby of the Scripps OBS Instrumentation Pool; and J. Nimblett, F. Raheem, and S. Scharf for assistance during the cruise. I express my gratitude to Seiich Nagihara, Jim Gaherty, Tim Long, Bob Lowell, Jean Stieglitz, Andrew Newman, Yingfei Yi, Irina Sokolik, and Peter Munch. I am deeply grateful to many compassionate friends in Atlanta and Houston; my special thanks go to Seva, Changsub, Taehyun, Youngdal, Yunsu, Lt. Kim, Dr. Yang, Dr. Song, Gill-Ran, Amy, Tatiana, Scott, Sara, JFK, Tim, Rob, Tom, Kremena, Alice, Maya, Kathy, and other friends for their endless encouragement.

TABLE OF CONTENTS

LIST OF TABLES

LIST OF FIGURES

SUMMARY

The Far-Offset Active-Source Imaging of Mantle (FAIM) experiment was conducted along an 800-km-long transect in the Western Atlantic to study the evolution of 108-157 m.y. lithosphere. The main transect (Line 1) crosses a transition from slow (13-14 mm/yr in half rate) to ultra-slow (~8 mm/yr) paleo spreading rates, and thus represents an ideal setting to study spreading-rate dependent processes as expressed in lithospheric structure. This thesis presents results of four analyses efforts along this transect. We present a crustal model based on seismic refraction and wide-angle traveltime modeling, we extend the crustal model to an upper lithosphere density model using gravity constraints, we constrain Poisson's ratio in oceanic Layer 3 using converted shear-wave phases, and we consider regional lithospheric structure by analysis of geoid/topography ratios.

The crustal model indicates that a transition in crustal thickness accompanies the spreading-rate change, with the crust produced at slow rates being 1.0-1.5 km thinner. The gravity modeling shows that a density model can be constructed that simultaneously satisfies observed gravity, seismic constraints on crustal thickness, and our expectation of isostasy if ~1.3 km of low-density material is distributed into the upper 30-60 km of the mantle. This amount of material (~1.3 km) roughly equals the difference in thickness between slow and ultra-slow spreading crust, suggesting that that the thinner crust formed during very slow spreading arises due to melt retention in the mantle rather than decreased mantle melting. Modeling of mode-converted S-wave phases reveals a uniform Poisson's ratio (~0.27) in the lower crust. Along with the observation of sharp crust/mantle boundary, this result suggests that crust along the FAIM transect is primarily melt-derived igneous crust. Geoid versus topography relationships along Line 1 and nearby parallel tracks show abrupt changes that may originate from lateral changes in mantle density, possibly in response to the transition from slow to ultra-slow spreading. This type of observation may enable us to extend our inferences to a more regional scale.

CHAPTER 1

INTRODUCTION

1.1 Mid-ocean ridges and the formation of oceanic lithosphere

In 1855, US navy lieutenant Matthew Maury published a bathymetric chart revealing the first evidence of underwater mountains in the central Atlantic. Later, the presence of these mountains, the Mid-Atlantic Ridge (MAR), was confirmed while the first trans-Atlantic telegraph cable was being laid. The East Pacific Rise (EPR) was discovered during an H.M.S *Challenger* cruise in 1875. We now know that the global mid-ocean ridge system extends ~70,000 km and represents the divergent boundaries of plate tectonics. The present day spreading rates of mid-ocean ridges vary between approximately 5 and 100 mm/yr. The fastest spreading ridge today is the portion of the EPR between the Nazca and Pacific plates with a half spreading rate of ~100 mm/yr.

Oceanic lithosphere consists of the basaltic oceanic crust (~6 km thick) and the portion of the upper mantle that defines Earth's upper thermal boundary layer. Oceanic lithosphere begins its evolution, or is "formed", at a mid-ocean ridge. The processes of lithospheric formation at mid-ocean ridges, or mid-ocean ridge processes, are important to our understanding of mantle dynamics. These processes include mantle upwelling in response to plate separation, decompression melting as hot mantle rocks pass through the solidus, melt extraction and focusing toward the ridge-axis crustal-accretion zone, the formation of oceanic crust (solidification of melt), and the cooling and subsidence of the lithosphere as it moves away from the plate boundary. Morphologically, the mid-ocean ridges are underwater mountain ranges. The topographic elevation of the ridges is caused

by the greater buoyancy of the thinner, hotter lithosphere near the axis of the ridge crest. The elevation of the ridge provides a body force that helps to drive the lithosphere away from the spreading center. This phenomenon is referred to as "ridge push", and it is one of the important forces driving the plates [*Turcotte and Schubert,* 1982].

We have a mature model of mid-ocean ridge processes based on a number of geological, geophysical, and geochemical studies [e.g., *Grove et al,* 1992; *Forsyth,* 1993; *MELT experiment team,* 1998], but we still have a limited knowledge of the pattern of mantle flow beneath spreading centers [*Forsyth,* 1992], the mechanisms of melt extraction and focusing toward crustal accretion zones [*Turcotte, and Morgan,* 1993], and the processes that lead to thinner oceanic crust when spreading is relatively slow [*Reid and Jackson,* 1981]. Two end-member models of divergent-boundary mantle flow have been proposed [e.g. *Forsyth,* 1993], each with different implications for melt production and extraction processes. In the passive-flow model, mantle flow is driven solely by the spreading plates, and a broad region of mantle upwelling and melt production is predicted. In this case, melt is focused toward ridge axis by pressure gradients induced by viscous stresses. In the active-flow model, solid mantle flow is driven both by the plates and by buoyancy forces induced by lateral variations in melt content [i.e. *Spiegelmen and Reynolds,* 1999]. In this case, the melt region is relatively narrow, and melt extraction is primarily vertical. Our understanding of the conditions under which one or the other of these mechanisms dominates continues to evolve as geophysical experiments continue to probe lithospheric structure diagnostic of these processes.

Oceanic lithosphere preserves structure inherited at the mid-ocean ridge as it moves away from the spreading center. This structure can be imaged or detected with various

geophysical methods and used to infer aspects of mantle dynamics operating in the past. For example, seismic refraction techniques may measure changes in crustal thickness. These changes can be related to the volume of extracted melt at the mid-ocean ridge in the past, and one may infer that such a variation relates to varying melt production or melt-extraction efficiency. Similarly, a lateral change in mantle composition might be inferred from marine gravity anomalies or geoid versus topography relationships requiring a lateral density variation. Such a change may be caused by a varying degree of melt depletion or the presence of trapped melt. Mantle flow induces shear deformation and alignment of anisotropic minerals. Aspects of this alignment can be measured seismically to infer mantle flow patterns, as was done with data from the MELT experiment [*MELT experiment team,* 1998]. The fact that structures originating from mid-ocean ridge processes are preserved below the seafloor has practical implications for geophysical studies. Seismic imaging in older lithosphere is generally easier than at hot, melt rich, hydrothermally active spreading centers, and imaging structure in old oceanic lithosphere provides information on past mantle dynamics and provides a means of targeting processes likely to occur under particular conditions – a change in spreading rate, for example.

In this study, we are interested in gaining insight into the role of spreading rate in lithosphere formation. We have analyzed seismic and marine gravity data collected during the Far-offset Active-source Imaging of the Mantle (FAIM) experiment (Figure. 1.1) conducted in the western Atlantic. The main transect of this experiment extends 800 km along a plate-kinematic flow line and crosses lithosphere spanning 108-157 m.y. in age (Figure. 1.1). Paleo-spreading rate changes significantly along this transect,

providing an opportunity to investigate the spreading rate-dependence of mid-ocean ridge processes.

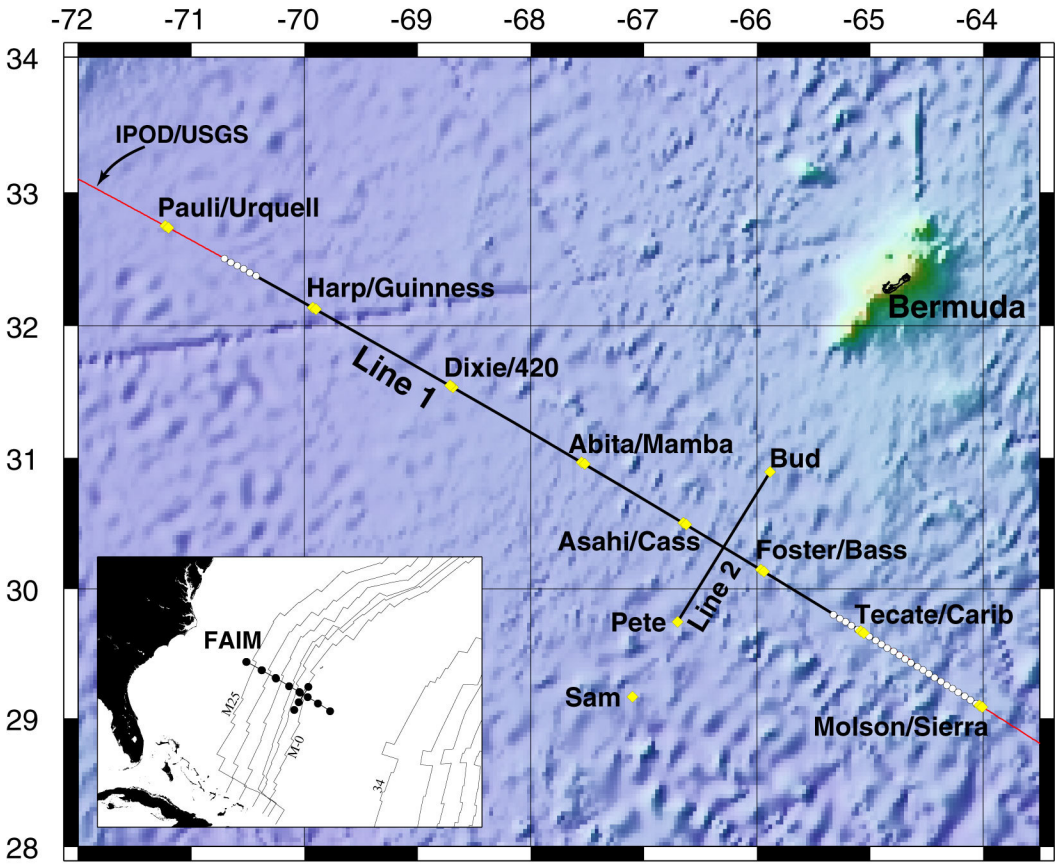

Figure. 1.1 FAIM experiment location map. OBS locations indicated by diamonds, circle-shot locations by white circles. Line 1 follows the IPOD/USGS transect.

The primary result of this study is that many observations such as changes in crustal thickness, basement topography, upper-mantle density, geoid-versus-topography relationships, and mantle P-wave propagation correlate with a transition from slow to ultra-slow spreading. We explore an explanation for this correlation that involves melt retention due to less efficient melt extraction at slower spreading rates. In Chapter 2, we provide details of the FAIM experimental setting and discuss results of modeling wide-

angle seismic data and marine gravity collected along the main transect (Line 1). These results define crustal-thickness and mantle-density variations along Line 1. In Chapter 3, we present results of modeling mode-converted S-waves. These results constrain Poisson's ratio in the lower crust and upper mantle and suggest that the lower crust is gabbroic, with negligible degree of serpentinization. This conclusion supports a straightforward relationship between crustal thickness and retained melt inferred from mantle density and seismic velocity estimates. In Chapter 4, we analyze geoid versus topography relationships in an effort to extend of our inferences to a regional scale.

In the remainder of this introductory chapter, we briefly review aspects of active-source marine seismic methods, describe the general character and seismic velocity structure of oceanic crust and lithosphere, review marine gravity observations, and comment on the seafloor topography (bathymetry) of the study area.

1.2 Marine seismic methods

There are two types of seismic waves, body waves and surface waves. In this study, we only make use of body waves. Body waves can be further divided into P- and S-waves. P-waves are characterized by particle motions in the medium parallel to the direction of the propagation. P-waves can be detected by pressure sensitive hydrophones suspended in the water column or geophones that respond to displacements of the seafloor. The particle motion of S-waves is normal to the direction of travel. The propagation velocity of these waves is less than that of P-wave velocity in the same medium. The ratio of P- and S-wave velocity is related to Poisson's ratio, which is the topic of the Chapter 3 in this thesis. Since fluid does not have rigidity, S-waves are not

observed in water, but they may be detected using ocean bottom seismometers (OBS) or borehole geophones.

Active-source marine seismic exploration involves three main elements: a seismic source, a means of detecting and recording seismic waves, and a method of analyzing the recorded data. Seismic sources for offshore investigation fall into two categories: impulsive, which provide a short lived burst of elastic wave energy, and swept-frequency, which produce an approximately sinusoidal signal of longer duration and progressively varying frequency. Impulsive sources are widely employed at both small (< 5 km) and large source-to-receiver offsets, often in excess of 100 km. Swept-frequency devices are less common. Chemical explosives generate broadband, high-energy pulses. Because of concerns about damage to marine life and the inherent danger in firing at frequent time intervals required to obtain structural detail, towed sources that are activated every few seconds have been developed. They produce seismic energy in a variety of ways, including the vibration of piezoelectric or magnetostrictive material, the rapid expansion of a gas bubble, the collapse of a steam bubble, and a sudden electrical discharge. For high seismic resolution, deep-towed and seabed sources have been built, the latter capable of generating shear as well as compressional waves. Source signatures, spectra, the efficiency of energy conversion and variation in output with direction vary considerably between these different source types. The choice of source is governed by the seismic resolution and penetration required. The sudden discharge of compressed air into water by airguns produces a short, high-energy seismic pulse [*Ewing and Zaunere,* 1964]. Airguns are the most commonly used source for seismic profiling at sea, replacing earlier devices that depended on the ignition of explosive gases or the release of

superheated steam into water. One of the technical achievements of the FAIM experiment is the demonstration of long-range propagation of P-waves emanated from an array of airguns through the mantle to depths of ~30 km. A more detailed account for how this was accomplished is given in Chapter 2.

Seismic waves are detected by the pressure variations they produce within the water column and by ground motions at the seabed. The former are recorded with hydrophones made from a piezoelectric material, such as barium titanite. Hydrophones are normally placed in arrays, which can be fixed, free floating or towed. Geophones consisting of a movable coil-magnet assembly, respond to displacements of the seafloor. Fixed bottom receivers have been widely used for marine seismic investigations and were used in the FAIM experiment.

1.3 Oceanic lithosphere and seismic velocity structures

The outer shell of the earth, the lithosphere, remains rigid during intervals of geologic time, but the rock beneath the lithosphere is sufficiently hot so that solid-state creep can occur, leading to a fluid-like behavior on geologic time scales. The oceanic lithosphere represents three-fifths of the outermost shell of the earth and has been created during the last 160 Ma at mid-ocean ridges. Sedimentation occurs throughout the ocean, thus over a long period of time the rugged and faulted topography generated at mid-ocean ridges is buried under the sediments. The almost flat regions of the seabed, thousands of kilometers in width and some 5-6 km below sea level, are called abyssal plains. The FAIM experiment was conducted above the *Hatteras* abyssal plain in the Western Atlantic.

Oceanic seismic refraction experiments in the 1950s and by the 1960s had made a sufficient number of crustal seismic velocity measurements to show that, unlike continents, oceanic crustal structure varies little. These earlier works [i.e. *Raitt,* 1963] established that typical oceanic crust consists of four characteristic layers. Subsequent improvements in the marine seismic techniques have provided some refinement to this basic structure, suggesting a discontinuous series of velocity gradients in which the velocity increases with depth.

Geophysicists in the late 50's and early 60's [*Raitt*, 1963; *Hill*, 1957] suggested a canonical oceanic crustal structure consisting of four layers representing average seismic velocity stratification. Layer 1 is the sedimentary layer that thickens with distance from the ridge axis. The P-wave velocity at the top of the sediments is generally close to 1.5 km/s but increases with depth as the sediments become consolidated. At the top of Layer 2, the volcanic layer, there is a sudden increase in P-wave velocity to approximately 4 km/s. Reflection profiling has shown that the top of Layer 2, the oceanic basement, is very rough for crust that was formed at slow-spreading ridges. It was proposed in the 1970s that Layer 2 is probably best described as a region of the oceanic crust in which seismic velocity increases rapidly with depth [*Raitt*, 1963; *Purdy and Ewing*, 1986]. Drilling into the top of Layer 2 has shown that it is made up of sediments, basaltic lavas and lava debris in varying degrees of alteration and metamorphism [i.e. *Wyllie*, 1976; *Bratt and Purdy*, 1984]. Deeper drilling has found more consolidated basalts [*Bratt and Purdy*, 1984]. Some dykes that cause a further increase in P-wave velocity were found near the base of this layer [*Bratt and Purdy*, 1984]. Layer 3 is thicker and much more uniform than Layer 2. Typical P-wave velocities in Layer 3 are 6.5-7.0 km/s, with

gradients of around 0.1 km/s per kilometer depth [*Hill*, 1957; *Raitt*, 1963; *Purdy*, 1983]. Layer 3 is generally presumed to be gabbroic in composition. Some seismic experiments have shown that the basal part of this layer has higher P-wave velocities (7.2-7.7 km), indicating perhaps a change to more cumulate-rich gabbros at the base of the crust. *Hess* [1962] proposed that Layer 3 is partially serpentinized peridotite, formed as a result of hydration of the upper mantle. Actually, a number of lithologies have been proposed for Layer 3 [*Raitt,* 1963].

Ophiolites, a sequence of rocks characterized by basal ultramafics overlain by gabbro, dykes, lavas and deep-sea sediments, are often regarded as samples that bear a close resemblance to shallow oceanic lithosphere. They, however, may be atypical of normal lithospheric lithology in that they are now tectonically emplaced on land, and the crust in the ophiolites may be created in the back-arc basins behind subduction zones. Ophiolites occur in such locations as Cyprus, Newfoundland, Yemen, and New Guinea. Field studies of ophiolites have provided a detailed understanding of the oceanic crust and underlying mantle [*Fowler,* 1990].

One well-studied ophiolite is the Semail ophiolite in the Sultanate of Oman. The Semail ophiolite is believed to have been formed some 95 Ma ago at a spreading center in the Tethyan Sea and later emplaced on the Arabian plate as Tethys closed when Africa and Arabia moved northwards and collided with Asia. The seismic velocity structure of these rock units is similar to that of the oceanic crust and upper mantle, with a gradient through Layer 2, a rapid increase in velocity at the Layer 2/3 boundary [*Fowler,* 1990], and a relatively high velocity region at the bottom of the crust. The transition from crust to mantle in these ophiolites is sharp.

Ophiolites also preserve melt migration features formed in conductively cooled lithosphere as well as in adiabatically rising asthenosphere. One example in the Oman ophiolite is dunites in the mantle section (peridotites) [*Kelemen et al,* 1995]. Dunites comprise 5 to 15 % of the exposed mantle section in Oman. They preserve sharp, irregular contacts that are locally discordant to banding and crystallographic lineations in the peridotites. Additionally, pyroxenites and gabbro dykes are observed in the mantle section of many ophiolites. The dykes are generally undeformed, and highly discordant to the high temperature foliation in residual peridotites [*Kelemen et al,* 1995]. The formation of pyroxenites and plagioclase in the dykes is indicative of crystallization from an evolved, low-temperature liquid. Such an evolved liquid forms from a parental, mantle-derived magma as a result of crystal fractionation due to conductive cooling [*Kelemen et al,* 1995]. Consequently, it has been inferred that dykes in the mantle section of ophiolites formed off-axis, in oceanic lithosphere with a conductive geotherm [*Kelemen et al,* 1995]. In Chapter 2, we partially base our interpretation of modeling seismic data and marine gravity on these observations.

The seismic P-wave velocity of the uppermost oceanic mantle averages 8.1 km/s [*Purdy,* 1983]. The oceanic crust/mantle boundary may be a sharp transition, but it can have a finite variable thickness and is often a thin gradient zone. It marks the transition from the gabbroic crust to the peridotitic mantle. As with all seismic and geologic boundaries, there is some uncertainty about the exact correlation between the seismic boundary and the petrological boundary. The Moho is a seismic boundary, and presumably it is the transition downward into ultramafic rock. Petrologists conventionally distinguish between zones of cumulate ultramafic rock (such as dunite,

which is made of olivine), which have precipitated from a melt, and the underlying deformed residual upper mantle known as tectonite ultramafic.

1.4 Marine gravity and bathymetry

Earth's gravitational acceleration, *g* (referred to as gravity hereafter), is affected by changes in the mass (density) distribution below the sea floor, thus measurements of gravity at sea provide an important means of studying offshore regions. Since Earth is not a perfect sphere, the acceleration due to gravity varies from about 9.83 m/s^2 in the polar region to approximately 9.78 m/s^2 at the equator. In general, Earth's geometry and density structure, latitude, elevation and time-dependent distortions of the earth brought about by tidal forces all influence gravity. For comparison of measured gravity worldwide, we must compare these values with the geoid, a surface on which the gravitational potential remains the same and which can be roughly defined as mean sea level. Consequently, measured values of gravity at sea arising from mass differences below sea level can be isolated and used to infer the density distribution. In this thesis, gravity is expressed in milliGals (mGal), equal to 10^{-5} m/s^2, because the residual field comprises only a small part of the total gravity.

Gravity is measured using a gravimeter, and there are three different types [*Jones,* 1999]. Spring gravimeters consist of a beam or other mass supported by springs. In some sensors the moving mass is constrained to motions in the vertical direction and are free of coupling effects between horizontal and vertical acceleration. Vibrating-string gravimeters have a sensing element in the form of a suspended string or fiber set subject to natural vibration, the frequency of which is related to gravity. Gravity changes are

derived from variations in string frequency. Forced-feedback instruments have two permanent magnets being counteracted by a feedback system that keeps the mass in a null position. Acceleration is sensed by the displacement of this mass suspended between magnets. Gravity is measured from electric current variations in the feedback circuits. During the FAIM experiment, we used a forced-feedback instrument, the BGM-3 gravimeter manufactured by the Bell Aerospace Company, consisting of a forced feedback accelerometer mounted on a gyro-stabilized platform on the *R/V Maurice Ewing*. The gravimeter outputs raw counts approximately once per second which are logged and processed to provide a real-time gravity display during the cruise as well as adjusted gravity data at the end of the cruise.

Water depth is a fundamental observation in the ocean, and it is essential for oceanographic and geophysical studies. The short wavelength components of marine gravity anomalies are largely influenced by seafloor topography, thus it is necessary to obtain precise bathymetry for modeling gravity. The longest wavelength of bathymetry is governed by thermal subsidence of the lithosphere, as newly created plates move away from the mid-ocean ridge and get denser and cooler. Ocean floor structure with horizontal scales of 10 to a few hundred kilometers and vertical scales of 100 m or more generate sea surface gravity anomalies observable with satellite altimetry [*Smith,* 1998]. It is suggested that the topographic roughness of mid-ocean ridge flanks increases with decreasing spreading rate [e.g. *Lonsdale,* 1994] and scales with lithospheric thickness [*Malinverno,* 1991]. *Smith* [1998] argued that the fine scale (10-80 km) roughness of old ocean floor is spreading-rate dependent in the same way that it is at mid-ocean ridges,

suggesting that fine-scale tectonic fabric is also generated nearly exclusively by ridge-axis processes.

In the Western Atlantic, including the vicinity of the FAIM site, many investigators have noted a change in the character of acoustic basement from "smooth" to "rough" in the western North Atlantic basin west of the Bermuda island [e.g. *Vogt et al,* 1971; *Sundvik et al,* 1984]. In the study area, the presence of this boundary is obvious along Line 1 and approximately coincides with the location of instrument *abita* (Figure. 1.1). In Chapter 2, we demonstrate that the changes in seafloor topography correspond to spatial changes in crustal and mantle structure, revealing that the smooth seafloor is underlain by thicker crust and overlying mantle with a negative P-wave velocity gradient, whereas the rough portion of the transect overlies thinner crust and mantle with a positive mantle velocity gradient.

CHAPTER 2

ANALYSIS OF SEISMIC DATA AND MARINE GRAVITY

2.1 FAIM experimental setting

The FAIM seismic experiment consisted of two transects. The first transect, Line 1, is an 800-km-long transect oriented along a flow line within a single spreading segment. This transect coincides with the IPOD/USGS multi-channel seismic (MCS) reflection line [*Grow and Markl,* 1977], enabling us to use those data to constrain depth to the basement. Sixteen short-period vertical-component, 2-Hz ocean-bottom seismometers (OBS) were deployed (Table 2.1) in 3-km-separated pairs along Line 1. The eight OBS pairs along Line 1 were spaced 80-120 km apart (Figure. 1.1). Line 2 is perpendicular to Line 1, is 150 km long, and had an OBS deployed at each end of the line. The OBSs recorded shots fired from a 20-element, ~150-liter airgun array towed behind the R/V *Maurice Ewing*.

Table 2.1 Deployment positions in deployment order, relocated seafloor positions, distance to pauli, and depth.

Name of instrument	Deployment position	Seafloor position	X to pauli (km)	Depth (m)
sam	29.1667 -67.1022			5170
harp	32.1367 -69.9263	-69.934 32.136	139.296	5419
guiness	32.1235 -69.8984	-69.905 32.123	142.385	5384
pauli	32.7474 -71.2296			5408
urquell	32.7343 -72.2012			5415
dixie	31.5493 -68.7129			5248
420	31.5360 -68.6863	-68.685 31.535	274.894	5247
abita	30.9673 -67.5505	-67.554 30.967	399.585	5174
mamba	30.9528 -67.5230	-67.526 30.954	402.619	5133
asahi	30.5059 -66.6526	-66.655 30.507	499.578	5058
cass	30.4921 -66.6253	-66.627 30.493	502.608	5063
pete	29.7444 -66.7005			5176
bud	30.8937 -65.8839			4896
foster	30.1468 -65.9660	-65.968 30.147	576.715	5005
bass	30.1328 -65.9395	-65.941 30.133	579.743	4996
tecate	29.6788 -65.0908	-65.09 29.677	676.176	5048
carib	29.6587 -65.0526	-65.05 29.657	680.632	4926
sierra	29.0833 -64.0043	-64.012 29.086	799.578	4967
molson	29.0976 -64.0305	-64.035 29.099	796.917	4961

The FAIM experiment was designed to record mantle refractions at very large offsets. As described in *Lizarralde et al.* [2004], the experiment had two primary goals, to study basic upper mantle structure and to test shooting strategies that would enable airguns to be used at offsets of up to several hundred kilometers. The principal difficulty with using airguns in very large offset marine refraction surveys is previous shot noise (PSN) [*Nakamura et al.*, 1987], and the only complete solution to this problem is providing sufficient time between shots to enable all water-borne energy to travel past the seismometer at the farthest source/receiver distance. A second potential difficulty is refraction amplitudes that are smaller than ambient noise levels, and a solution to this problem can come from stacking multiple co-located shots. Therefore, two modes of shooting, "circle" shots and "on-distance" shooting were tested. The circle-shooting mode was tested on the eastern 150 km and western 36 km of Line 1. Circle shooting involved shooting many shots (between 17 to 36) at a prescribed shot interval while steaming in a 1-km-radius circle, the tightest possible with the towed source array. Static corrections were applied to the traces from each circle, and the traces were stacked in three bins per circle. The center of the circles were spaced 6 km apart, and so by merging the stacked circle shots from each 3-km-seperated OBS pair, profiles with clusters of 6 traces spaced of ~3 km apart were formed. Circle shots can be seen on the instrument *carib* and *sierra* profiles (Figure 1.1). On-distance shooting, with a shot spacing of 1 km and a corresponding shot interval of ~6 minutes, was used over the majority of Line 1. These source-points were revisited on multiple transits of portions of the line, with between 1 to 7 shots fired at each point, and the resulting co-located traces were stacked.

The 1-km trace spacing of the FAIM OBS profiles (Figure. 2.1) is somewhat sub-optimal for crustal-scale refraction analysis, but the signal/noise ratio is exceptional for marine profiles, enabling all relevant phases to be confidently identified and their travel times picked. Refractions through the sediments, oceanic Layer 2, and oceanic Layer 3 (P_g), as well as wide-angle reflections from the base of the crust (P_MP) are clearly observed on all of the profiles. Trace-to-trace coherence and good signal/noise ratios enable picking of these phases at a confidence of ~15 ms for all instruments except *carib* and *sierra*, where the larger trace spacing of the circle shots and the rough seafloor here makes phase correlation less obvious. In addition, the mantle refraction phase (P_n) is observed on the record sections of instruments deployed east of km 330 (in a coordinate system extending eastward from the western most instrument, *pauli*). As described in detail by *Lizarralde et al.* [2004], the P_n phase is absent on the record sections of the instruments deployed west of this location with the exception of *harp*, where the phase is observed over a ~25-km-long interval west of the instrument. *Lizarralde et al.* [2004] explain the P_n observations as an evidence of a transition in upper mantle velocity gradient, from zero or negative to positive, near the center of Line 1. A similar transition in crustal structure is observed at this location.

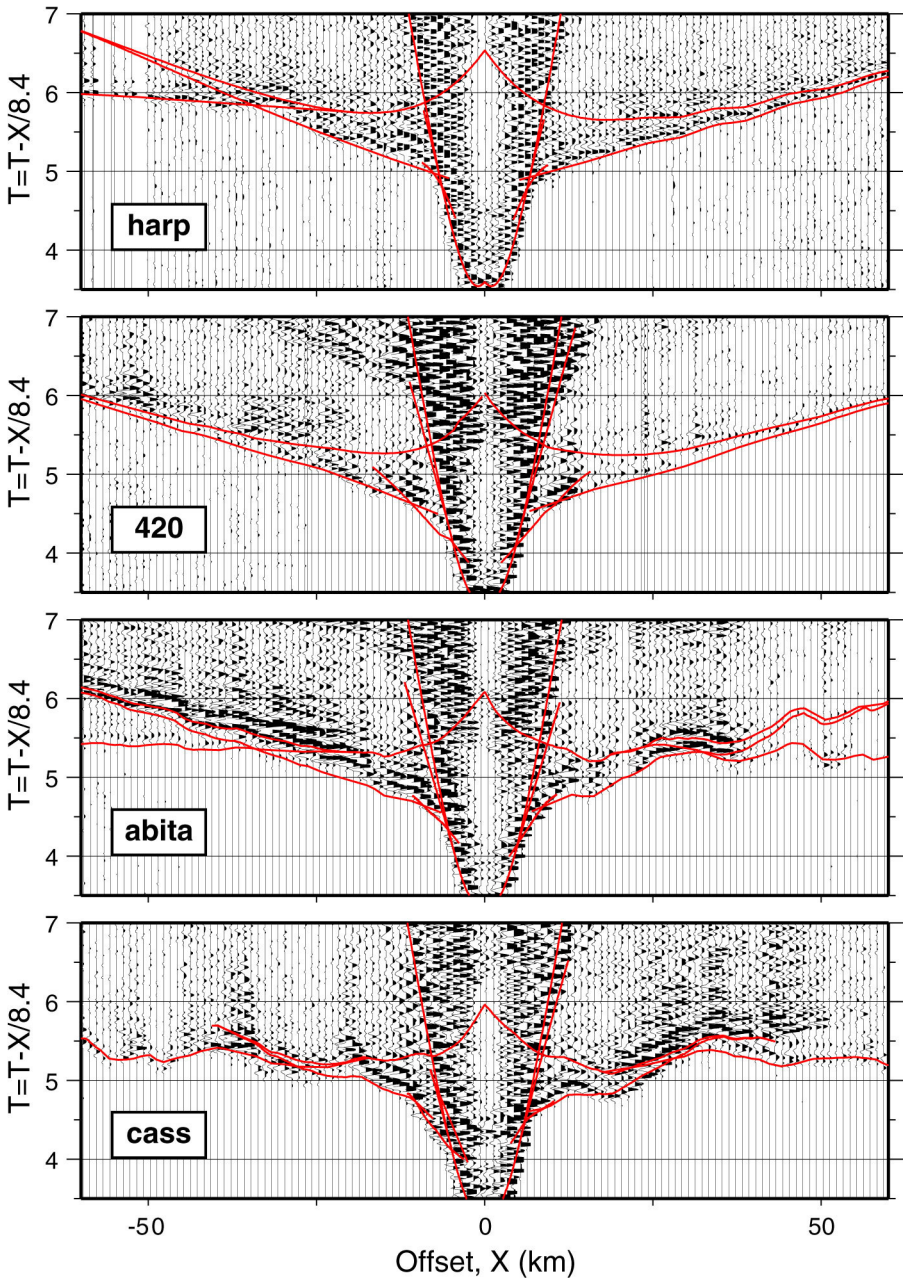

Figure. 2.1 Record sections displayed with reduction velocity of 8.4 km/s, offset amplitude scaling using a factor of $X^{1.2}$, and predicted travel time curves overlain. Circle shots are evident on instruments *carib* and *sierra*.

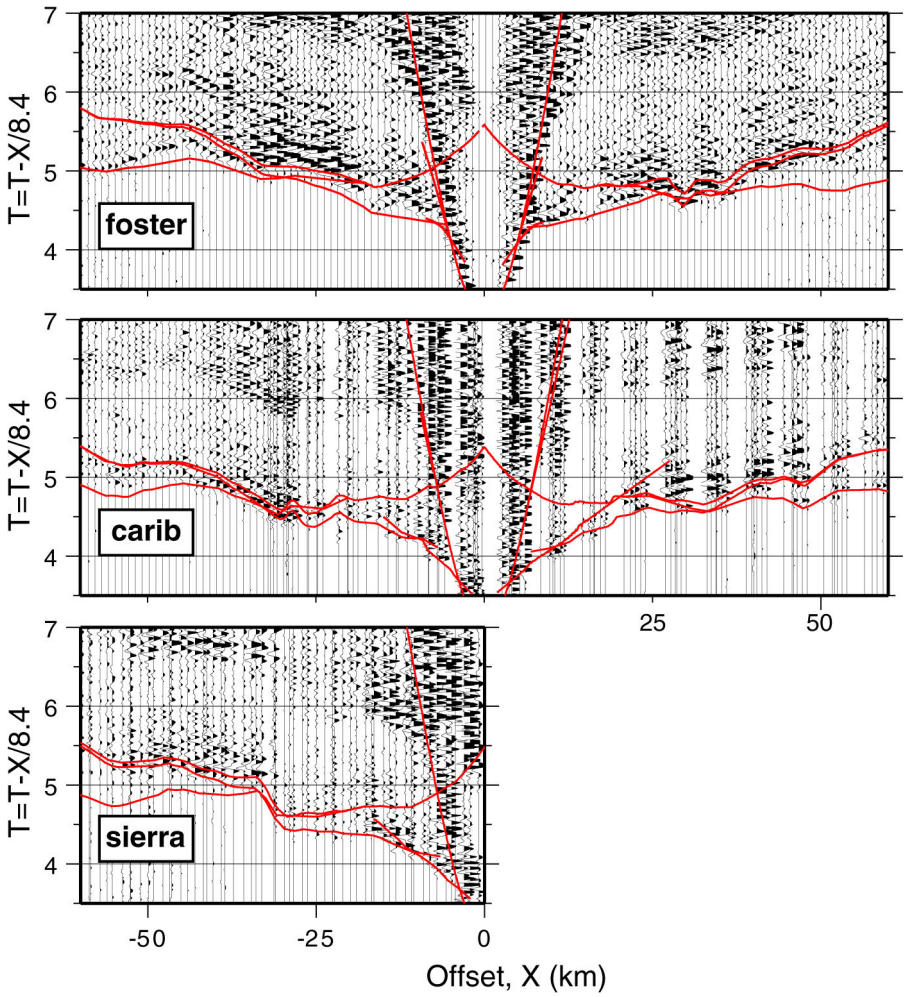

Figure 2.1 continued

2.2 Crustal structures from wide-angle seismic data

Measurements of oceanic crustal thickness have been an important source of information in deepening our understanding of mid-ocean ridge processes. Compilation of oceanic crustal thickness measurements [*White et al.,* 1992] have found an average thickness of oceanic crust of ~6.5 km for full spreading rates from 20 to 150 mm/yr. Crust of this thickness is predicted to be produced by the standard "passive flow" model via decompression melting of mantle with a potential temperature of ~1300°C, where

mantle upwelling is in response to plate separation and melt extraction is efficient [*Parson and Mckenzie,* 1978; *Mckenzie and Bickle,* 1988;*Bown and White,* 1994]. Therefore, observed crustal thickness appreciably different from the global mean thus suggests some deviation of MOR processes from those of simple passive flow model. Different mechanisms of mantle flow [*Sotin and Parmentier,* 1989; Cordery and Phipps Morgan, 1993], variation in mantle potential temperature [*Mckenzie and Bickle,* 1988], and varying efficiency of melt extraction [*Jha et al.,* 1994] may produce crust that is thinner or thicker than the global average. Spreading rate is a forcing function that affects these crustal-production processes [*Reid and Jackson,* 1981] in particular, crustal thickness at the slow end of the global spreading rate spectrum.

A number of observations indicate that crustal thickness decreases with spreading rate at full-spreading rates below 20mm/yr [*Reid and Jackson,* 1981;*White et al.,* 2001; *Jokat et al.,* 2003], the transition to so-called "ultra-slow" spreading [*Dick et al.,* 2003]. Exactly how spreading rate works to control crustal production remains uncertain. Conductive cooling and the presence of a thick thermal lid near the active spreading center are thought to be controlling factors. This lid inhibits shallow melting, resulting in thinner crust and a melting zone that is deeper on average [*Langmuir et al.,* 1993;*White et al.,* 2001]. Melt extraction may also be less efficient at slow spreading rates, as melt produced below the thermal lid may tend to freeze within the lid on the way to the surface, producing thinner crust and leaving behind a component of trapped, crystallized melt within the residual mantle [*Cannat,* 1993, 1996;*Kelemen et al.,* 2004; *Lizarralde et al.,* 2004]. Melt buoyancy may become an important component of upwelling at slower spreading rates [*Sotin and Parmentier,* 1989], affecting the pattern of mantle flow and

thus the shape of the melt zone and the dynamics of melt extraction [*Parmentier and Phipps Morgan,* 1990; *Cordery and Phipps Morgan,* 1993].

Constraints on crustal structure across a transition in spreading rate provide information on processes controlling crustal production. As mentioned in the earlier chapter, paleo-spreading rates along this transect range from slow (14 mm/yr half spreading rate) to ultra-slow (8 mm/yr) [*Klitgord and Schouthen,* 1986; *Muller et al.,* 1997] thus measurement along this transect inform us about changes in crustal production as spreading rate changes from the slow to ultra-slow. There have been very few crustal seismic experiments conducted on crust formed at ultra-slow spreading rates (half spreading rate < 10 mm/yr) [*Muller et al.,* 1997;*Klingelhofer et al.,* 2000;*Tolstoy et al.,* 1993;*Joket et al.,* 2003]. In this chapter, it is demonstrated that changes in crustal thickness are correlated with a transition from slow to ultra-slow spreading.

2.3 Modeling seismic data

We used a combination of forward and inverse modeling to obtain crustal velocity models at each OBS site along Line1. The large spacing between instruments along FAIM Line 1, with unreversed crustal phases, precludes two-dimensional modeling along the entire transect. We thus modeled the travel times of each OBS independently to obtain a crustal thickness estimate at each instrument location. Our modeling approach is quasi-two-dimensional, as we use hydrosweep bathymetry data and the migrated IPOD/USGS MCS profile to constrain two-dimensional seafloor and basement topography. For the igneous crust, however, we assume a nearly 1-D structure consisting of extrusive and intrusive layers (Layer 2 and Layer 3) with a horizontal interface

between them (implying a constant Layer-2/Layer-3 thickness ratio) and a planar but potentially dipping crust/mantle interface, or Moho. We assume that velocity gradients exist in these layers and that these gradients are laterally constant. The velocity of the sediments and the depth to basement are derived from the two-way travel time to basement observed in the MCS data using empirical velocity/depth relationships [*Carlson et al,* 1986]. Travel time constraints on sediment velocity only exist very near each OBS, but only minor adjustment (via forward modeling) to the empirically determined sediment structure was needed to satisfy these constraints. Similarly, a Layer 2 structure much like those obtained for other North Atlantic locations [*Purdy and Ewing*, 1986] satisfies the travel time constraints.

The seismic structure of oceanic Layer 3, or the lower crust, was determined by travel-time inversion for a three-parameter model. The parameters are the depths to a planar Moho at 100 km distance on either side of the instrument and the average velocity of Layer 3 assuming a fixed vertical gradient. This parameterization results in a laterally uniform Layer-3 velocity everywhere except near the Moho. We used a velocity gradient based on *Purdy* [1983], a seismic study conducted on the IPOD/USGS transect coincident with FAIM Line 1. This gradient is consistent with other measurements of North Atlantic crustal velocity [*White et al.,* 1992]. Fixing the average-velocity, we inverted for the Moho depth parameters using the P_g, P_MP, and P_n travel times and the inversion code of *Zelt and Smith* [1992], with upper mantle velocities from *Lizarralde et al.* [2004]. By repeating this procedure for a suite of average velocities, a best-fitting model under this parameterization was found for each instrument, and a model misfit

curve was produced that reflects the sensitivity of crustal thickness beneath the instrument to velocity.

The misfit curves shown in Figure 2.2 provide a means of estimating the uncertainty of the crustal thickness estimates. The RMS error of the best fit models, summarized in Table 2.2, ranges from 34 ms (*420*) to 89 ms (*cass*). The principle source of misfit is short-wavelength variation in the travel times arising from short-wavelength crustal-structure variation that cannot be constrained with existing data or captured with the model parameterization. The range of variation in RMS error between instruments is similarly explained by variability in crustal complexity along the transect. The smoothest basement surface along the transect is found near *420*, for example, and basement topography is most extreme near *cass*. To estimate uncertainty from the misfit curves, some cutoff value of significant misfit must be chosen. The choice can not be based simply on some factor of the misfit of the best-fit model, however, because of the correlated nature of the travel time data. In Figure 2.3, for example, we show the predicted travel times of the best fitting model (RMS=34 ms) for OBS *420* and of a model with a misfit ~1.5 times this value (RMS=85 ms). The fit of the later model is clearly much poorer, with systematic, correlated misfit indicative of incorrect crustal velocities. The RMS value at which travel time misfit becomes visibly poor is ~35 ms above the RMS misfit of the best fitting model. This is true for all of the instruments, since they share similar crustal phases, frequency content and ranges, resulting in the similar build up of long-wavelength systematic error regardless of the background short-wavelength error of the particular instrument. Using 35 ms above the minimum value as a significant level of misfit, we estimated crustal-thickness uncertainties as indicated in

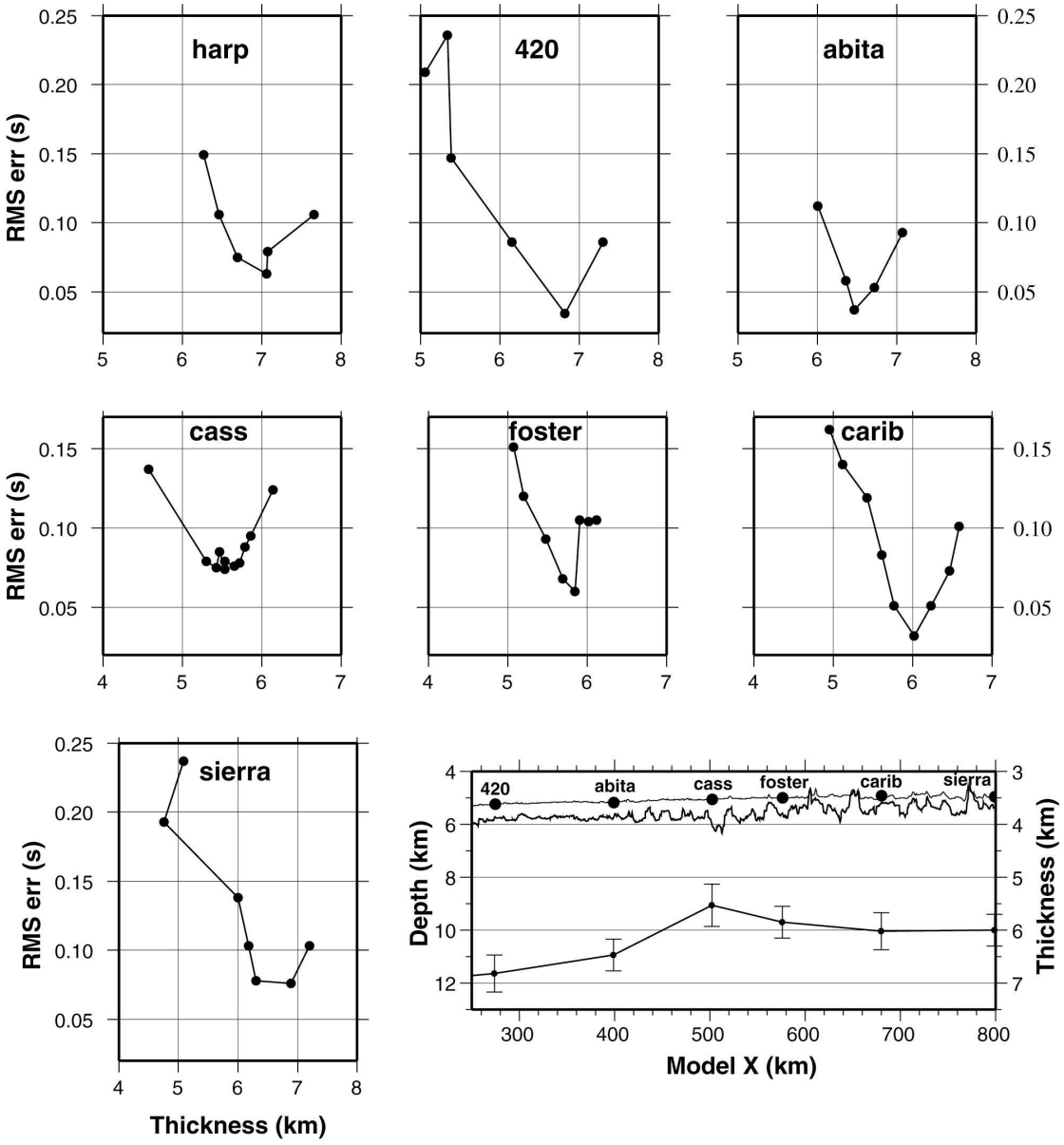

Figure. 2.2 Misfit versus igneous crustal thickness directly beneath each instrument for models with a constant Layer-3 velocity-gradient obtained by fixing average Layer-3 velocity and inverting for Moho depth and dip. Igneous crustal thickness uncertainty estimates are based on a significance threshold 35 ms above the minimum misfit value for each instrument. Bottom right: Bathymetry and basement depth plotted using the Depth axis, crustal thickness with the Thickness axis. Note the transition in crustal thickness near the center of the transect.

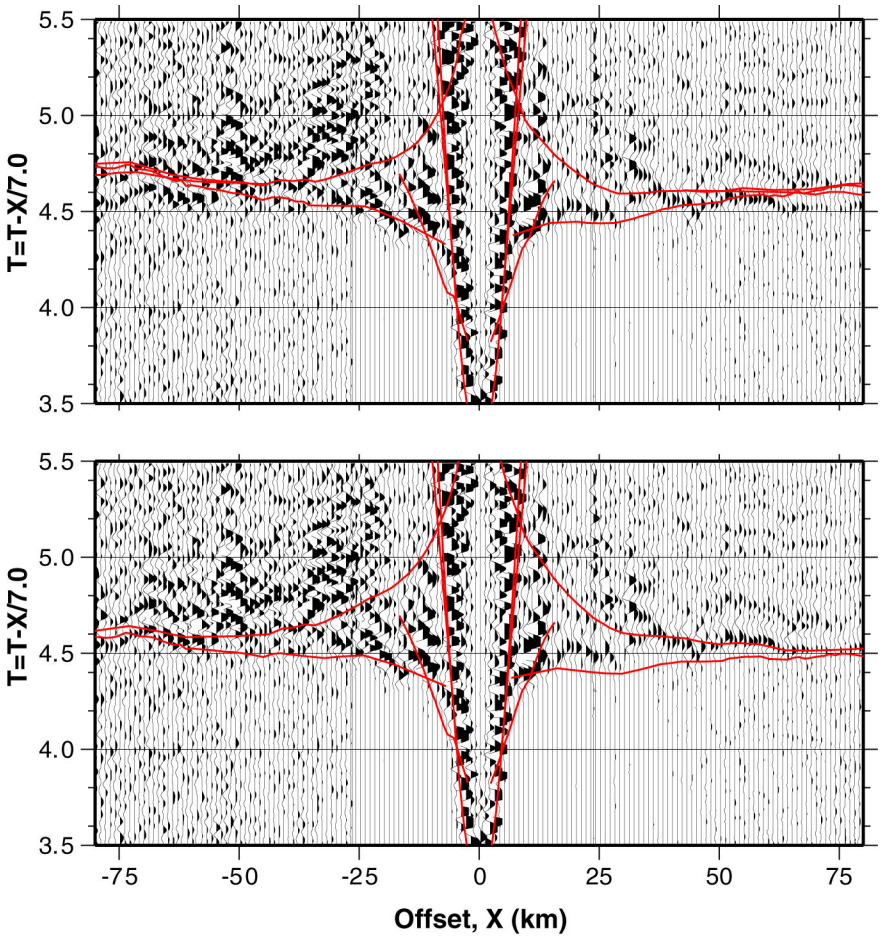

Figure. 2.3 OBS *420* predicted travel times from the best-fit model (bottom) with an average Layer-3 velocity of 6.95 km/s, and a model with an average Layer 3 velocity of 6.85 (top) on the record sections of the instrument 420. The systematic misfit of the later travel times indicates incorrect Layer 3 velocity, and so a significant misfit level must lie below the 50-ms misfit difference of these two models.

Table 2.2. Crustal thickness uncertainties are mostly 0.2-0.3 km, except for *cass*, which, by our criterion, has an uncertainty of 0.7 km. OBS *cass* exhibits considerable insensitivity to average velocity, however, yielding similar crustal thickness for most reasonable values of velocity, and this suggests a somewhat better thickness estimate than the ±0.7 km based on our criterion.

Table 2.2 Location and water depth of each instrument along with RMS travel time misfit of the best fitting model and crustal thickness, thickness uncertainty.

Instrument	*harp*	*420*	*abita*	*cass*	*foster*	*carib*	*sierra*
Model offset (km)	139.2	274.8	399.5	502.6	576.7	680.6	799.5
Water depth (km)	5.41	5.24	5.17	5.06	5.00	4.92	4.96
RMS travel time misfit (s)	0.064	0.034	0.038	0.089	0.060	0.052	0.078
Crustal thickness (km)	7.06	6.82	6.47	5.53	5.85	6.02	6.30
Thickness uncertainty (km)	0.32	0.30	0.20	0.70	0.20	0.22	0.30
Average Layer 3 velocity (km/s)	6.85	6.95	6.85	6.95	6.95	6.95	6.95

The average lower-crustal velocity of the best fitting model for each instrument is similar, ranging from 6.85 km/s to 6.95 km/s. Crustal thickness, however, varies along the transect (Table 2.2). The two instruments west of km 400 (*harp*, *420*) have an average crustal thickness of 6.94 km; at km 400 (*abita*) crustal thickness is 6.47 km; and east of km 400 (*cass*, *foster*, *carib*, *sierra*) average crustal thicknss is 5.86 km. We emphasize km 400 because a transition from slow (west of km 400) to ultra-slow spreading (east of km 400) occurs here, and we note that the crust east of km 400 is 1.0-1.5 km thinner than crust to the west.

2.4 Modeling Gravity

The distribution of instruments along FAIM Line 1 is sparse, and so it is useful to consider observed gravity anomalies to help interpret the seismic measurements of crustal thickness. In many crustal seismic studies, it is common that a density model can be found that satisfies observed gravity with only minor adjustments to seismically

determined structure and assumed velocity/density relationships. This is not the case for the gravity anomalies along Line 1. We consider several simple models based on bathymetry, basement topography, seismically determined crustal structure, and isostasy considerations, and we find that it is necessary to adjust the upper mantle density structure in order to satisfactorily fit the observed gravity anomalies.

The first density model we consider has a crustal structure based on the seismic constraints, and we refer to it as the "seismic-crust" model. The seafloor is constrained by hydrosweep bathymetry, and basement is constrained by the sediment/basement interface as observed in the IPOD/USGS MCS profile. The Moho is defined by interpolation between the crustal thickness estimates beneath each OBS location except between km 425-475, between *abita* and *cass*, where we have thinned the crust to account for the steep gravity-anomaly gradient and gravity high in this location. We note that the shape of this imposed Moho conforms to patterns in both basement morphology and spreading rate (Figure. 2.4). For the densities of the sediments and oceanic Layers 2 and 3, we used 2100, 2800, and 2950 kg/m^3. Mantle density structure is defined by a thermal structure obtained using a plate-cooling model incorporating spreading rate changes, a 200-km-thick plate, and a potential temperature of 1300°C, with a coefficient of thermal expansion of 3.28×10^{-5} °C^{-1}, and a mantle density of 3300 kg/m^3 at 0°C. The thermal plate parameters were chosen to fit the bathymetry of the sediment-unloaded basement.

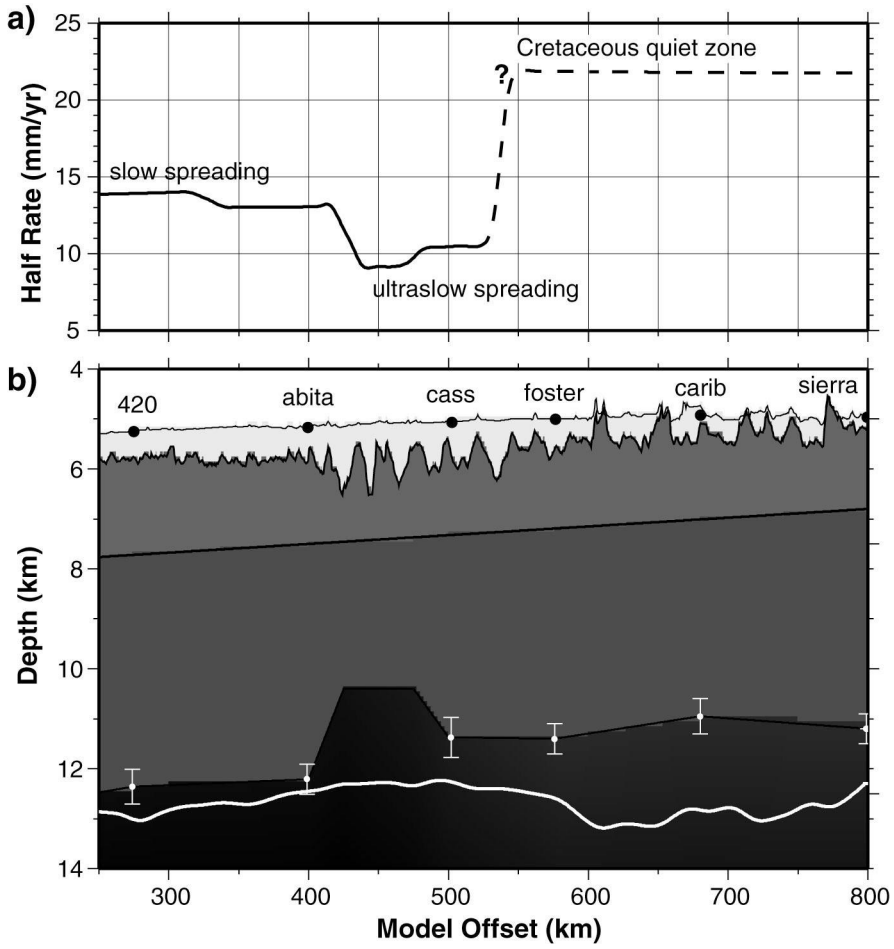

Figure 2.4 a) Spreading rate along Line 1 from *Müller et al.* [1997]. The Cretaceous quiet zone (CQZ) begins east of km 545, and the local spreading rate here is not known. The mean rate for the CQZ is indicated as a dashed line. Rough oceanic basement suggests that spreading was slower than this average, however. b) Crustal model illustrating crustal thickness constrained by seismic measurements (dots with error bars) and gravity modeling, and the predicted Moho for Airy isostatic equilibrium (continuous white line). The gravity data require thin crust in the interval km 420-475 where the slowest spreading takes place and where no OBS data exist.

The gravity anomaly predicted for the seismic-crust density model, curve in Figure 2.5b, has a large misfit (~14 mGal) with respect to the observed anomaly, with a positive over prediction of the anomaly suggesting too much mass near the surface. This large misfit challenges the appropriateness of our crustal model, and so we constructed a second model where crustal structure is defined so as to satisfy isostasy. The seismic-crust model is not in isostatic equilibrium. The white line just beneath the Moho in Figure 2.5 indicates the position of the Moho for a crust that is in isostatic equilibrium. Modifying our initial density model using this isostatically defined Moho, we created a second model which we refer to as the "isostatic-crust" model (Figure 2.5c). The isostatic-crust model has nearly constant thickness along the transect, and it would provide a poor fit to the seismic data. The fit of the predicted gravity for the isostatic-crust model (Figure 2.5b) is also poor, with an RMS error of ~7 mGal. The misfit indicates that there is too little mass in the eastern portion of this model, suggesting that a model intermediate between the seismic-crust and isostatic-crust models should be considered.

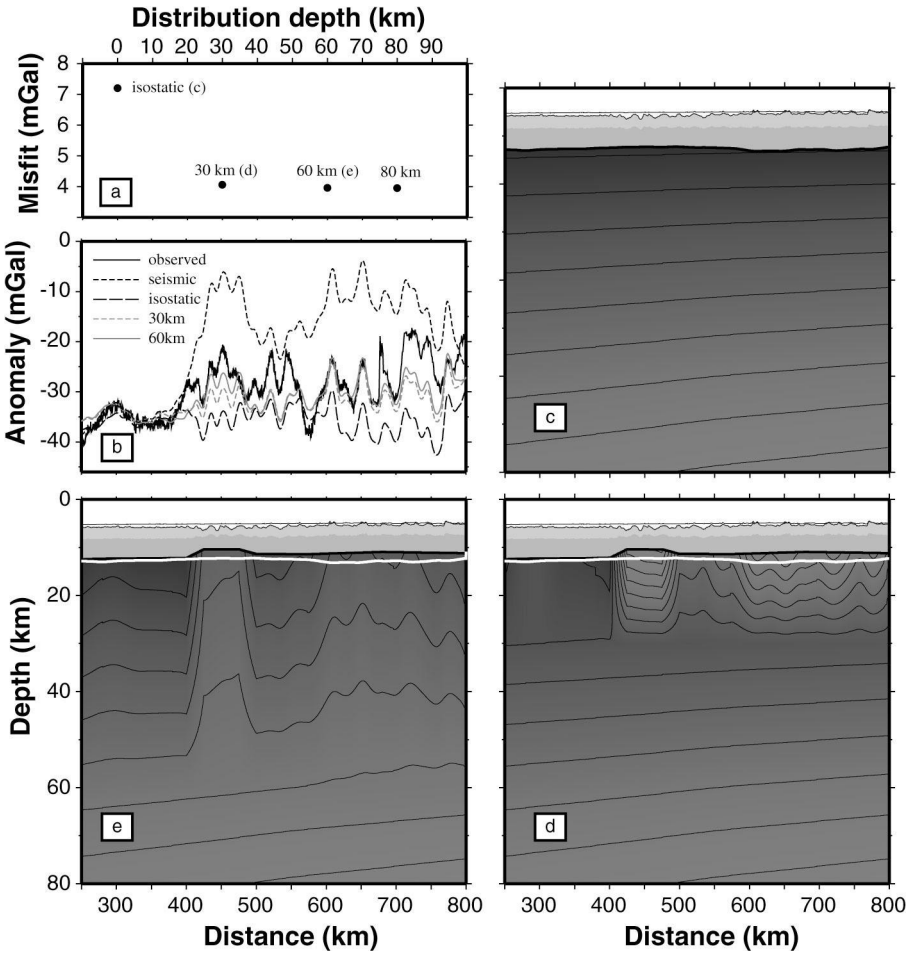

Figure 2.5 a) Misfit, in terms of RMS error, of predicted gravity for the "isostatic-crust" model and models with a "seismic" Moho and low density material distributed between 30-, 60- and 80-km depth and the Moho. Misfit for the "seismic-crust" model is 14 mGal. b) Predicted gravity for the various models. The fit of the "seismic" and "isostatic" models is poor. c) "Isostatic-crust" model, with crustal thickness determined to be in equilibrium with a cooling-plate lithospheric mantle. d and e) Models with a "seismic" Moho, but with low density material distributed between 30 km and 60 km depth so as to satisfy isostasy. White line is the "isostatic" Moho.

We constructed a third type of model from the first two. This model uses the seismically defined crust, thereby satisfying these constraints, and it satisfies our

expectation of isostasy and the need for less mass in the east by decreasing the density of the underlying mantle. The change in mantle density is equivalent to taking the amount of crustal material (2900 km/m^3) that lies between the "seismic" and "isostatic" Moho (~1.3 km beneath the eastern half of the transect) and distributing it over some depth interval below the seismic Moho, mixing the crustal material with mantle material. We consider several cases, with material distributed from starting depths of 30, 60 and 80 km up toward the Moho, with the amount of added crustal-density material increasing linear upward from zero at the starting depth (Figures. 2.5d & e). These models each yield good fits to the observed gravity (Figures 2.5a & b). A model with less dense material beginning at 30 km depth yields an RMS misfit of 4.1 mGal, and models with material beginning at 60 and 80 km have RMS misfits of ~3.1 mGal. We believe that there is no significant difference in misfit at RMS values below ~5 mGal due to the three-dimensionality of basement structure. We estimated this significance level by computing the RMS difference between the observed satellite-derived gravity along Line 1 and along transects parallel to Line 1, 10 km north and south of the line. The RMS difference between these nearby transects is ~5 mGal, manifest primarily in wavelengths associated with basement topography. This suggests that on the order of 5 mGal of variation could exist in the observed anomaly along Line 1 due to three-dimensional basement topography. Misfit of our 2D gravity model below ~5 mGal is thus not significant.

Density models that satisfy the seismic constraints on crustal thickness, observed gravity, and our expectation that the lithosphere is near isostatic equilibrium require low density material distributed over some depth interval between ~30-80 km depth and the Moho beneath the thinner crust of the eastern half of FAIM Line 1. These density

models exhibit a fairly abrupt lateral transition in vertical density gradient towards the center of the model near the location of the change from slow to ultra-slow spreading rate. As described below, a similar lateral transition in vertical seismic velocity gradient has been inferred to occur near this same location by *Lizarralde et al.* [2004] based on the propagation properties of mantle refractions. They interpret this transition to indicate a change in melt extraction processes attending the spreading-rate change. Applying this interpretation to our gravity models, the low density material beneath the eastern portion of the transect would be ascribed to melt retained at the ridge during lithosphere formation, now present in the residual mantle as gabbroic inclusions.

2.5 Discussion

Compilations of global oceanic crustal thickness measurements indicate that crustal thickness decreases systematically with spreading rate for full spreading rates less than 20 mm/yr [*Reid and Jackson,* 1981; *White et al,* 1992]. This decrease in crustal thickness with spreading rate has been explained by two main mechanisms: a decrease in total melt production due to the increasing influence of the thermal lid and consequent decrease in melt-column height above the solidus [*White et al,* 2001; *Bowen and White,* 1994], and less efficient melt extraction, also due to the influence of the thermal lid, but via mechanisms that remain uncertain [*Cannat,* 1996; *Lizarralde et al,* 2004]. There is also a correlation between increasing incompatible element concentration in crustal rocks and decreasing crustal thickness for spreading rates below 20 mm/yr [*White et al,* 2001]. *White et al.* [2001] show that this correlation can also be explained by a shorter melt column, since melts formed at greater depth are generally more enriched in incompatible

elements. This explanation for crustal thickness and geochemisty systematics with spreading rate is attractive because of its simplicity. It does not, however, incorporate any aspects of a wide melting zone [*Plank and Langmuir,* 1992; *Spiegelman and Reynolds,* 1999], probably involving a distributed melt network [*Spiegelman and Kelemen*, 2003], and it does not address the new observations presented here, which provide evidence for a melt-retention/spreading-rate systematic for ultraslow spreading.

We observe a change in crustal thickness near the center of FAIM Line 1 that is correlated with a change in spreading rate from slow to ultraslow (Figure. 2.5). We also find that observed gravity along the transect is best fit with density models that include low density material in the upper mantle beneath the thinner crust generated during slower spreading. If the low-density upper mantle beneath the thinner (slower spreading) crust in the east results from a mixture of gabbro and peridotite, then the amount of gabbroic material (~1.3 km) present in the mantle of the density models roughly equals the difference in thickness between the measured crustal thickness and the crustal thickness needed to satisfy isostacy (1.0-1.5 km, Figure 2.5).

The lateral change in vertical gradient in our density models is similar to the laterally varying velocity gradient that *Lizarralde et al.* [2004] invoke to explain FAIM mantle refraction observations. They find that the mantle beneath the thicker (faster spreading) crust does not propagate mantle refractions, presumably due to the lack of a positive velocity gradient, while that beneath the thinner (slower spreading) crust does, indicating the existence of a positive velocity gradient. *Lizarralde et al.* [2004] infer that the transition in vertical velocity gradient is due to a change in the amount of melt retained in the mantle, and that this change is controlled by spreading rate. The

observations presented here confirm that less crust was produced over the eastern portion of the transect, and that the west-versus-east (or slow-versus-ultraslow) crustal-thickness difference may exist in the mantle as gabbroic inclusions, reflecting melt retention at the mid-ocean ridge. Taken together, these results suggest that spreading rate plays a role in the melt extraction processes of slow-spreading systems, and that it may be provide more sensitive control on crustal thickness than total melt production (crustal thickness plus integrated mantle gabbroic component), which appears to remain nearly constant.

The FAIM results suggest that the sensitivity of melt-extraction processes to spreading rate effectively controls crustal thickness variation at slow to ultra-slow spreading rates. There are a number observations that suggest relatively large percentages of melt are commonly retained in the mantle at slow spreading rates, including geochemical evidence for fractional crystallization over depth ranges of up to 18 km [*Grove et al,* 1992], abundant plagioclase peridotites dredged from slow-spreading seafloor [*Dick*, 1989] that may represent residua of mantle fractional crystallization processes [*Grove et al,* 1992], and samples recovered from the ODP Leg 209 near the mid-Atlantic ridge that contain gabbroic rocks and mineral assemblages that indicate crystallization beginning at 15 to 20 km below the seafloor [*Kelemen et al,* 2004]. Still, a hypothesis that systematically links spreading rate and crustal thickness with melt retention must also account for the observed systematic geochemical variation with decreasing spreading rate, where thinner crust is found to be enriched in incompatible elements [*White et al,* 2001]. We thus consider possible relationships between melt geochemistry and the efficiency of melt extraction.

Lizarralde et al. [2004] describe a conceptual model that relates decreasing spreading rate and crustal thickness to increasing mantle melt retention and crustal incompatible element concentrations as a consequence of a thickening thermal lid. This model, illustrated in Figure 2.6, assumes a wide sub-axial melt zone, characteristic of passively driven mantle flow [*Forsyth,* 1993], that is drained by a network of high permeability melt conduits [e.g. *Kelemen et al.*, 1995].

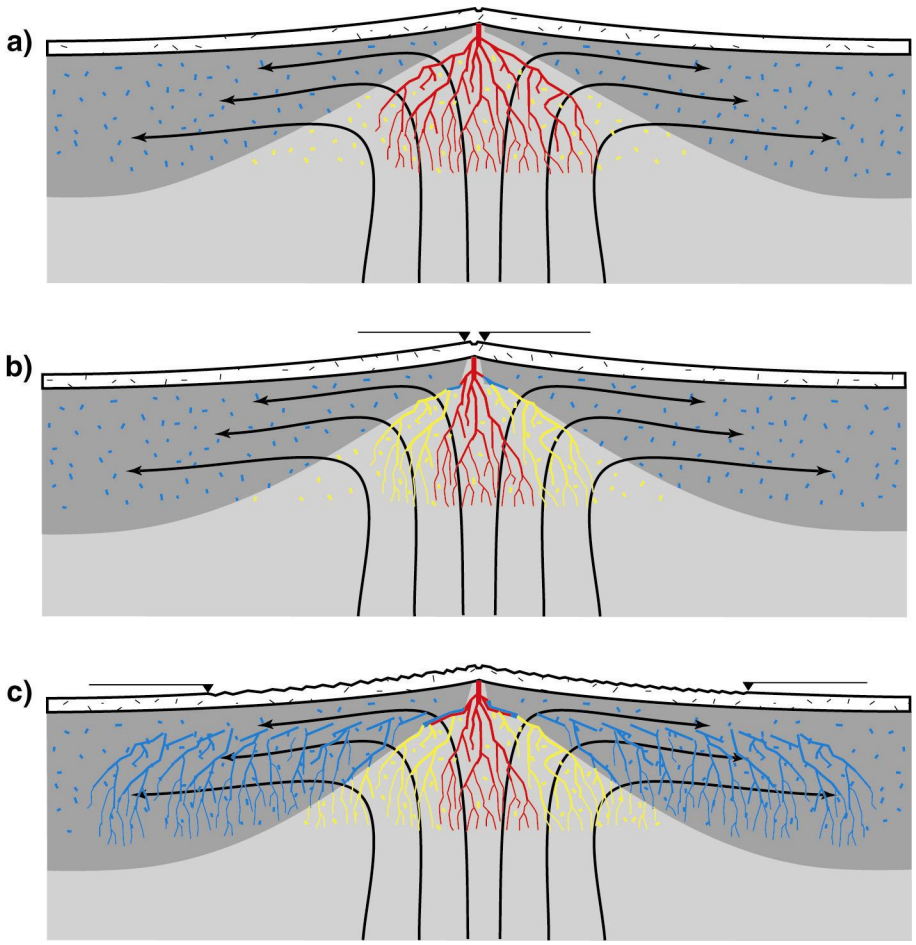

Figure 2.6 Conceptual model of increased melt retention accompanying a decrease in spreading rate. a) Lithospheric separation drives flow (arrows) with a broad (>100 km wide) melt (red) zone. Melt extraction occurs via a channelized melt network that

focuses melt to the ridge. Some melt (yellow) is not incorporated into the network and eventually crystallizes as gabbroic inclusions (blue). b) Thickening of the thermal lid due to a decrease in spreading rate (at triangle) affects channels that drain the off-axis portion of the network, trapping melt in that area. c) Trapped melt (yellow) eventually crystallizes (blue) into the lithosphere as it moves farther off axis. Melt that reaches the ridge originates from upwelling mostly beneath the spreading center.

The crust produced at the spreading center is an aggregate of melt from the entire melt zone, but *Spiegelman and Reynolds* [1999] showed that melt from different portions of the melt zone are likely to have different incompatible element concentrations. Melts that have traveled to the ridge axis from the greatest distance, "off-axis" melts, will tend to be diluted in incompatibles relative to "on-axis" melts that have traveled mostly vertically from directly beneath the ridge axis. *Lizarralde et al.* [2004] suggest that as the thermal lid thickens with decreasing spreading rate, it will tend to disrupt the conduits draining the off-axis portions of the melt zone, leaving these melts retained in the mantle and resulting in a thinner crust with increased incompatible element concentrations due to the dominance of on-axis melts. Extraction of on-axis melts is aided by the advection of heat, which would inhibit the formation of a thermal lid where melt is focusing near the spreading center.

Efforts to model melt extraction beneath mid-ocean ridges have aimed to explain how melt focuses from a broad melt zone into the narrow crustal-accretion zone at a spreading center. These models are thus concerned with getting melt out of the system rather than keeping melt in, but they are nevertheless instructive when thinking about

melt retention. In the conceptual model described above, off-axis melts are retained by crystallization of melt conduits, at the base of the thermal lid, that would otherwise drain melt from deeper in the melt zone. These off-axis conduits might be similar to the high-porosity channels showed by *Sparks and Parmentier* [1991], based on compaction considerations, to form between the melt zone and an impermeable crystallization front. *Montési et al.* [2002] showed that similar channels form along the base of an inclined thermal lid when reactive instability [*e.g. Ahranov et al,* 1995] plays a dominant role in the channelization of permeable pathways.

If the melt zone is drained by a network of channels formed through reactive transport [*Spiegelman et al.*, 2001], then the work of *Spiegelmen and Kelemen* [2003] suggests that a systematic relationship between decreasing crustal production and increasing crustal incompatible element concentrations may be a general consequence of shutting such a system down under the increasing influence of a thermal lid. *Spiegelmen and Kelemen* [2003] show that the center of dissolution channels contain trace-element-enriched melts from depth, while the edges of the channels transport highly depleted melts extracted from the inter-channel regions at shallow levels. As spreading rate decreases and the thermal lid extends farther into what had been the melt zone, channels will rely more heavily on advected heat from deeper melts to remain permeable while the contribution of shallow, inter-channel melts progressively diminishes. Thus, the observed crustal thickness/geochemical systematics with decreasing spreading rate may arise without the need to invoke a special role for high-porosity channels at the distal edges of the melt zone.

A separate mechanism of melt retention is the tapping of melt by cracks within the mantle. Gabbro-filled dykes extending 10 km or more into the mantle are a common feature of the upper mantle section of the Oman ophiolite [*Boudier and Coleman,* 1981; *Nicolas,* 1989], for example, and we might expect that low-temperature deformation mechanisms such as faulting and fracturing of the upper mantle become increasingly important as spreading rate decreases. *Gaherty et al.* [2004] suggest that this is the case along the FAIM transect. They show that upper mantle seismic anisotropy is approximately half of that observed in faster spreading Pacific lithosphere, and they explain this observation with an increased role for mantle faulting in accommodating extensional strain, as opposed to primarily viscous deformation that would lead to a lattice-preferred orientation of olivine grains. We can envision at least two ways that a fracture mechanism of melt retention might affect crustal incompatible element concentrations. First, the Oman mantle dykes appear to be undeformed by corner-flow processes [*Kelemen et al.,* 1995; *Braun and Kelemen,* 2002], implying that they formed off axis and are filled primarily with off-axis melts. As suggested above, any preferential retention of off-axis melts will tend to increase the incompatible element concentration of extracted melts. Second, by tapping off-axis melt, the off-axis melt zone may be robbed of the pressure head and the advected heat needed to establish and maintain a network of permeable channels via a reactive instability mechanism [*Ahranov et al.,* 1995], again leaving the off-axis melts stranded.

The mechanisms of melt retention considered above all invoke a wide melt zone characteristic of passively driven mantle flow. *Lizarralde et al.* [2004] point out that the preferential retention of off-axis melts with decreasing spreading rate, in addition to

providing a viable mechanism for melt retention that also explains the geochemical observations, provides an explanation for the observed spatial offset between the change in spreading rate along FAIM Line 1 and the lateral transition in vertical velocity gradient. This offset is a simple consequence of the width of the melt zone. It is important to point out, however, that a buoyancy-driven system can also produce the observed crustal thickness/geochemical systematics of slow to ultra-slow spreading. In these systems, both solid mantle and melt flow lines are tightly focused beneath the spreading center throughout the melt zone [*Speigelman and Reynolds*, 1999]. Melting within a buoyancy driven system can thus be thought of in terms of a single, vertical melting column that would behave much like the model (described above) that *White et al.* [2001] invoke to explain slow to ultra-slow spreading crustal observations. It follows that their model implies buoyancy driven, or "active" mantle flow beneath ultra-slow spreading centers. A principal result of the FAIM experiment is that several lines of evidence strongly suggest that melt retention in the mantle is also an outcome of decreasing spreading rate, and we are not able to think of a means by which a buoyancy-driven mantle flow system would progressively retain melt as spreading rate decreases. We thus infer that mantle flow, at least for the formation of the slow to ultra-slow lithosphere of the FAIM transect, was driven primarily by plate separatio

CHAPTER 3

POISSON'S RATIO ESTIMATES AND THE NATURE OF OCEANIC LAYER 3 ALONG THE FAIM TRANSECT

3.1 Poisson's ratio: Observations and applications

In Chapter 2, we demonstrated that a number of observations, including crustal thickness, mantle P-wave velocity structure, and gravity anomalies can be satisfactorily explained by melt retention occurring near the mid-ocean ridge as spreading rates become very slow. All of the observations are consistent with this explanation if the oceanic crust along Line 1 is made up of mainly melt-derived crustal rocks, enabling one to relate observed variations in crustal thickness to an amount of melt left frozen in the upper-mantle. However, serpentinized peridotite is commonly observed in slow-spreading settings [e.g. *Cannat,* 1996], and so it is possible that some portion of the measured crustal thickness along Line 1 may consist of altered upper mantle rocks. In this chapter, we attempt to assess this possibility by analyzing primary and multiply reflected mode-converted shear-wave arrivals observed in the FAIM OBS data. Shear-wave velocity, V_S, in combination with compressional-wave velocity V_P, provides substantially better indication of lithology than V_P alone. In particular, V_P for serpentinite and gabbro are quite similar (~6.6-6.7 km/s, *Christensen,* [1966]), whereas their Poisson's ratios are resolvably distinct, ~0.36 for pure serpentinite and ~0.28 for gabbro, [*Christensen,* 1996; *Brocher,* 2005].

Poisson's ratio is a material physical property defined as the radial contraction to axial elongation when the diameter of a cylindrical sample changes in the direction

normal to its length by tension or contraction along its axis (Figure. 3.1). Poisson's ratio, σ, is related to V_S and V_P as,

$$\sigma = 0.5\left(1 - \frac{1}{(V_P/V_S)^2 - 1}\right). \tag{3.1}$$

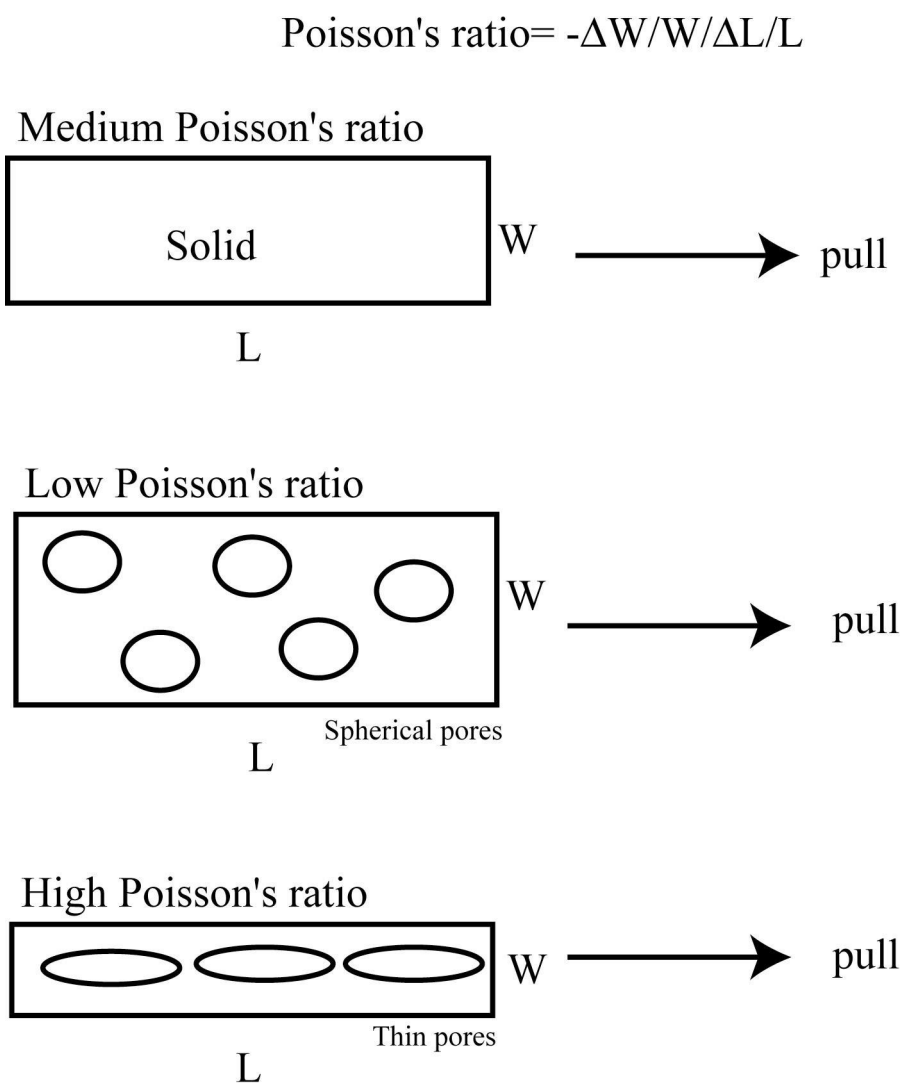

Figure 3.1 If a rock samples undergoes tension or compression along its axis, its diameter (W) will change in the direction perpendicular to its length (L). Poisson's ratio is the ratio of radial contraction to axial elongation. This figure demonstrates low and high Poisson's ratios due to the shape of pores in the rock samples.

Poisson's ratio for most solids varies from 0 to 0.5, and it is known to be better than V_p alone as an indicator of lithology. Dr. George Pickett, a researcher at Chevron during 1960's, demonstrated how V_P and V_S of various sedimentary rocks, when used together, segregated into distinct numerical ranges according to rock type [*Pickett,* 1963]. It was shown that both the elastic properties of the rock matrix and the physical properties of pore fluids affect P- and S-wave propagation and consequently Poisson's ratio. This observation can be explained by the differing propagation of P- and S-waves through porous media. Any change in either the rock matrix or pore fluid will create a discontinuity in the P-wave acoustic impedance of the rock system because P-waves travel through both elastic materials and fluids. Therefore, P-waves will reflect off boundaries where there is a change in either rock matrix or the pore fluid or both. In contrast, S-waves propagate through elastic media but not through fluids. Thus, only a change in the properties of the rock matrix creates a reflecting boundary for S-waves, and a change in the pore fluid will have only a very small effect.

In this study, mode-converted S-wave phases are analyzed to constrain lower-crustal and mantle lithology based on Poisson's ratio. It is thus relevant to review results of previous active-source seismic studies where V_S and Poisson's ratio of oceanic lithosphere were estimated. *Spudich and Orcutt* [1980] analyzed seismic refraction and wide-angle reflection data from the 1959 Fanfare cruise and identified three conditions that lead to efficient S-wave conversion in marine refraction experiment. First, P-to-S mode conversion is more efficient at a sharp velocity interface between regions of different velocity than at a broad velocity gradient between two regions, where broad and

sharp are defined with respect to seismic wavelength. Second, mode-conversion at a rough interface may significantly affect the coherence of resulting phases. When the amplitude of interface topography approaches a seismic wavelength or more, mode converted waves may be radiated incoherently from the interface. Third, P-to-S conversions are very strong at an unlithified-sediment/igneous-basement interface. The influences of a sharp interface on mode conversion were studied further by *White and Stephen,* [1980] using synthetic seismograms. They found that the interface between water or sediments and the volcanic basement was frequently the site of considerable mode conversion. Their simulations demonstrate that the efficiency of mode conversion decreases as sediment velocities are raised with a constant Poisson's ratio that is appropriate for consolidated sediments. An elevated σ in upper basement volcanic rocks may reflect weathering or the presence of rubble, cracks, or other void space in pillow lavas.

In early 1980's, there were studies of V_S of oceanic lithosphere based on OBS data in the North-east Pacific [*Cheung and Clowes,* 1981; *Au and Clowes,* 1984]. *Cheung and Clowes* [1980] analyzed three-component OBS data from three locations in the area northwest of northern tip of Explorer ridge and parallel to Revere-Dellwood fracture zone in the northeast Pacific Ocean. Their results, however, may not represent typical oceanic crust and upper mantle because both the V_P and V_S depth profiles in this area show no distinct seismic Moho and have an anomalously low upper-mantle V_P of ~7.4 km/s. This study found that Poisson's ratios vary considerably in the upper crust, but they are more consistent in lower crust, ranging from 0.26 to 0.31. Upper-mantle Poisson's ratios were inferred to be between 0.25 and 0.26. *Au and Clowes* [1984] present results from a wide-

angle seismic experiment using OBSs in the Nootka fault zone off the west coast of Canada. They derived a one-dimensional V_S-depth model by trial-and-error comparisons with WKBJ synthetic seismograms. Unlike previously constrained higher P_n anisotropy (~10%) in this area, V_S profiles show very weak SV anisotropy, with upper-mantle V_s being 4.5 km/s and 4.6 km/s in the direction approximately parallel to the spreading ridge and parallel to the direction of spreading, respectively.

Shaw [1994] developed a porosity-evolution model to explain age variation of upper oceanic crustal Poisson's ratio. Waveform inversion and compilations of published data [*Spudich and Orcutt*, 1980; *Au and Clowes*, 1984] indicate that anomalously low Poisson's ratios (as low as 0.24) occur only in the young (< 15 Ma) upper oceanic crust, but not in crust older than 60 Ma. According *Shaw's* [1994] crustal evolution model, in young crust, thin cracks are sealed by hydrothermal deposition to depths of several hundred meters, but thicker cracks remain unsealed at depths of 1-1.5 km. Therefore, a combination of sealed and unsealed cracks in younger crust may produce the observed anomaly in Poisson's ratio. As oceanic crust ages, this scenario predicts that deeper, thicker cracks gradually seal with increasing age by hydrothermal deposition, restoring Poisson's ratio to the laboratory values. *Shaw's* [1994] study was followed by wide-angle seismic experiments in the Pacific to constrain Poisson's ratios in younger oceanic crust [*Christeson et al.*, 1997; *Collier and Sing*, 1998]. *Christeson et al.* [1997] modeled P- and S-wave arrivals recorded by 45 OBSs to model regional structure of the 9°-10°N region of the East Pacific Rise (EPR). Modeling traveltimes of S-wave arrivals and waveform inversion of these data indicate highly variable Poisson's ratio within the upper crust, with values as low as 0.24, and a mean value of 0.26. They used the porosity

evolution model of *Shaw* [1994] to explain low values of upper crustal Poisson's ratio. *Collier and Sing* [1998] analyzed wide-aperture reflection data from the fast spreading EPR, determining the upper crustal Poisson's ratio of ~0.25. They ascribe variation in Poisson's ratio within the upper crust to a change in pore structure and/or a lithologic transition from extrusives to dykes.

A growing volume of field and laboratory data has enabled the development of empirical relationships between rock type and Poisson's ratio [e.g. *Christensen,* 1996; *Brocher,* 2005]. *Christensen* [1996] presents measurements of V_P and V_S of 678 rocks and divides them into 29 major groups for which velocity, V_P/V_S ratio, and Poisson's ratio are presented at several pressures. For common plutonic rocks, he identifies a clear trend relating Poisson's ratio to composition, in which Poisson's ratio for granitic rocks increases from 0.24 to 0.29 as composition changes to gabbro and then decreases with decreasing plagioclase and increasing olivine contents to 0.25 in dunite. It is mentioned that there is no simple correlation between Poisson's ratio and felsic and mafic rock compositions. This author however notes that a linear correlation of increasing Poisson's ratio with decreasing SiO_2 content is observed for rocks with 55 to 75 wt % SiO_2. *Christensen* [1996] indicates average Poisson's ratios for continental and oceanic crusts are 0.265 and 0.30, respectively. Similarly, *Brocher* [2005] derives nonlinear, multi-valued relations between V_P, V_S, and density for a wide variety of common rocks.

In this study, we are interested in constraining the lithology of Layer 3. *Hess* [1962] first proposed the possibility that serpentinized mantle rocks may be constituents of Layer 3. Serpentinization is an exothermic reaction involving the hydration of mantle rocks (peridotites). This reaction is capable of raising the rock temperature by about

260°C, if one ignores processes that lead to heat transport and cooling of the rock. Recently, it has been suggested that this reaction is the heat source driving the Lost City hydrothermal system [*Green,* 2005]. Changes in elastic properties with serpentinization are well documented for V_P by *Birch* [1960, 1961] and for V_S and Poisson's ratio by *Christensen* [1966]. As dunite (σ=0.25) is hydrated to serpentinite, there is a progressive change in Poisson's ratio to 0.36. Partially serpentinized dunites and peridotites have Poisson's ratios that fall between these limiting values and establish a well-defined relationship between Poisson's ratio, percent serpentinization, and density [*Christensen,* 1966, 1996; *Brocher,* 2005]. In section 3.3, we will base our interpretation of results of converted-wave modeling on this Poisson's ratio versus percent serpentinization trend.

Results of modeling various types of mode-converted S-wave phases observed on FAIM OBS profiles and an interpretation of those results are presented in the following sections. The major limitation to the estimation of Poisson's ratio from these data is that the OBSs used in the FAIM experiment had only a single, vertical component, and thus the recorded mode-converted phases are not simple P-to-S (or P-S) phases, but are, at a minimum, P-to-S-to-P (or P-S-P) converted phases (Figure 3.2).

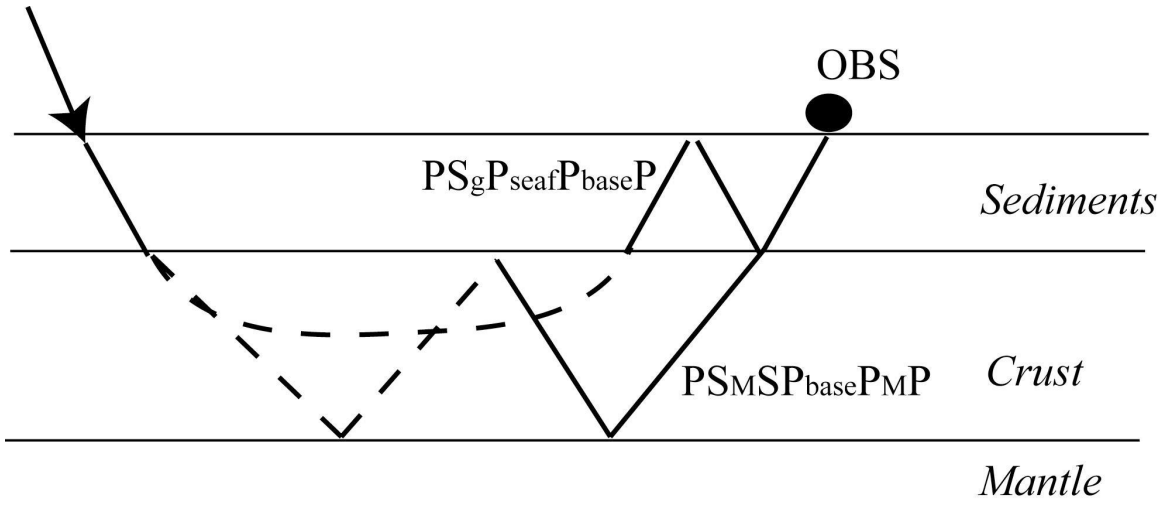

Figure 3.2 Typical multiply reflected converted phases registered on OBSs during the FAIM experiment. Solid and dashed lines are P-and S-wave segments of ray paths of S_g, S_MS, and S_n arrivals.

This more complicated conversion history generally results in some ambiguity in the travel path and conversion points as well as a reduced signal/noise ratio with respect to simpler P-S conversions. Nevertheless, some OBSs contain high enough signal quality to enable us to place constraints on Poisson's ratio in the crust and upper-mantle.

3.2 Observations

Among fourteen deployed OBSs, six instruments recorded mode-converted arrivals: *420*, *abita*, *carib*, and *tecate* along Line 1 and *bud* and *pete* on Line 2. Various crustal S-wave phases are recorded on *420* (Figures. 3.3 and 3.4), but no mantle phases – neither P_n

nor S_n, were identified. Figures 3.3 and 3.4 show primary and reverberated S_g and S_MS phases for instrument *420*. On *abita*, which was located near the smooth/rough seafloor boundary, the quality of the mode-converted data is marginal, and so this instrument was not used for modeling.

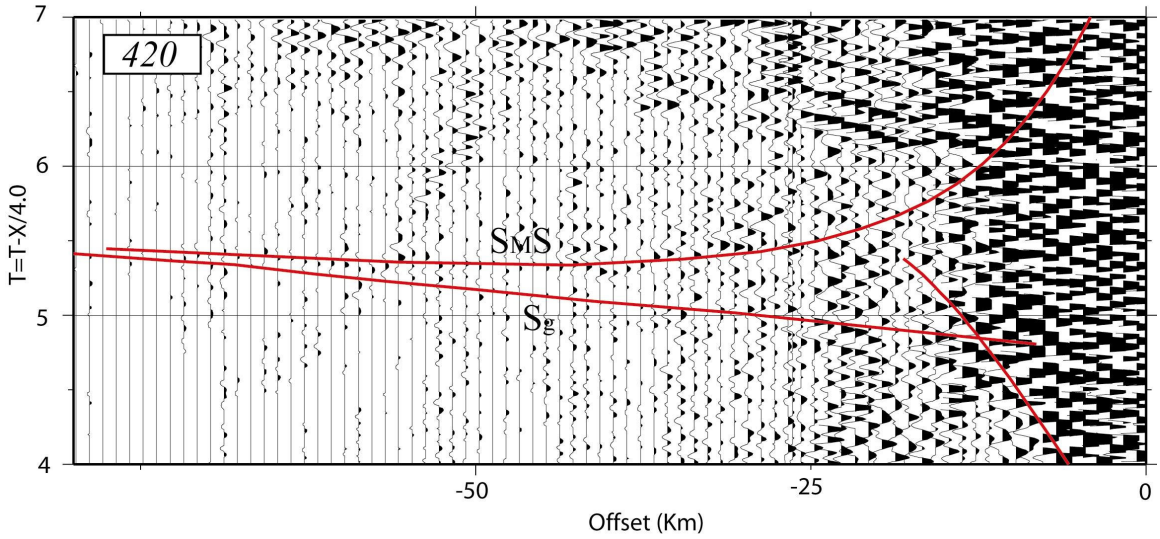

Figure 3.3 Mode-converted arrivals on *420* with negative offset. S_MS and S_g shown in this figure are multiply reflected phases described in figure 3.2.

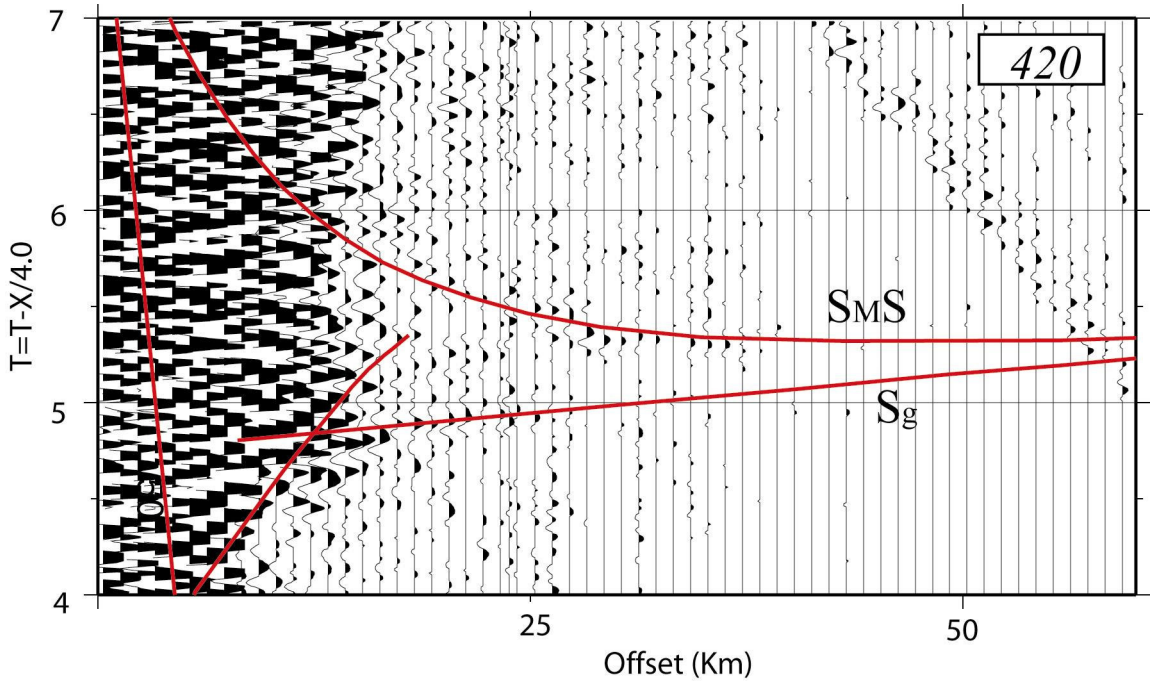

Figure 3.4 Mode-converted arrivals on *420* with positive offset. These arrivals are the multiply reflected waves of the types described in figure 3.2.

Instruments *carib* and *tecate*, which were deployed as a 3-km-separated pair on rough seafloor, both show clear expressions of the $S_g/S_MS/S_n$ triplication and its multiply-reflected variants (Figures. 3.5 and 3.6).

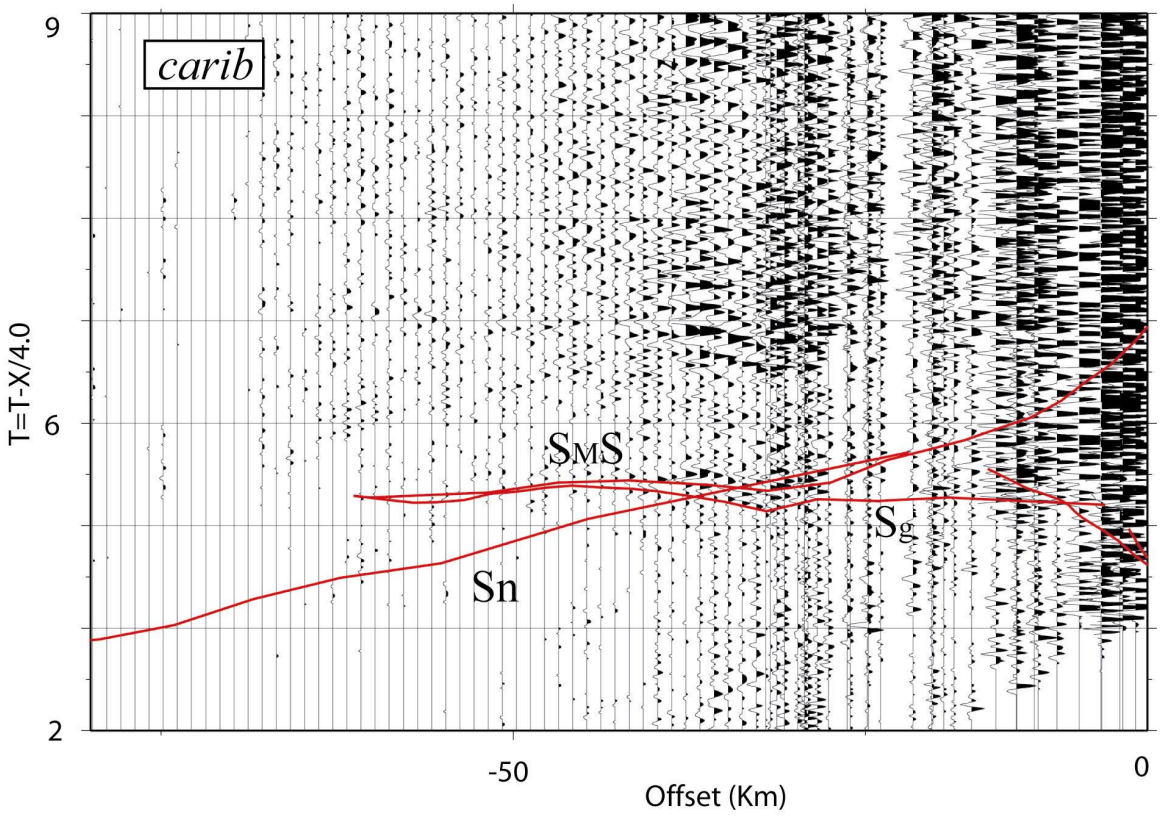

Figure 3.5 Triplication formed by S_g, S_MS, and S_n on *carib*. It shows obvious triplication of mode converted phases and its water column multiple near ~6.2 second in reduced time axis.

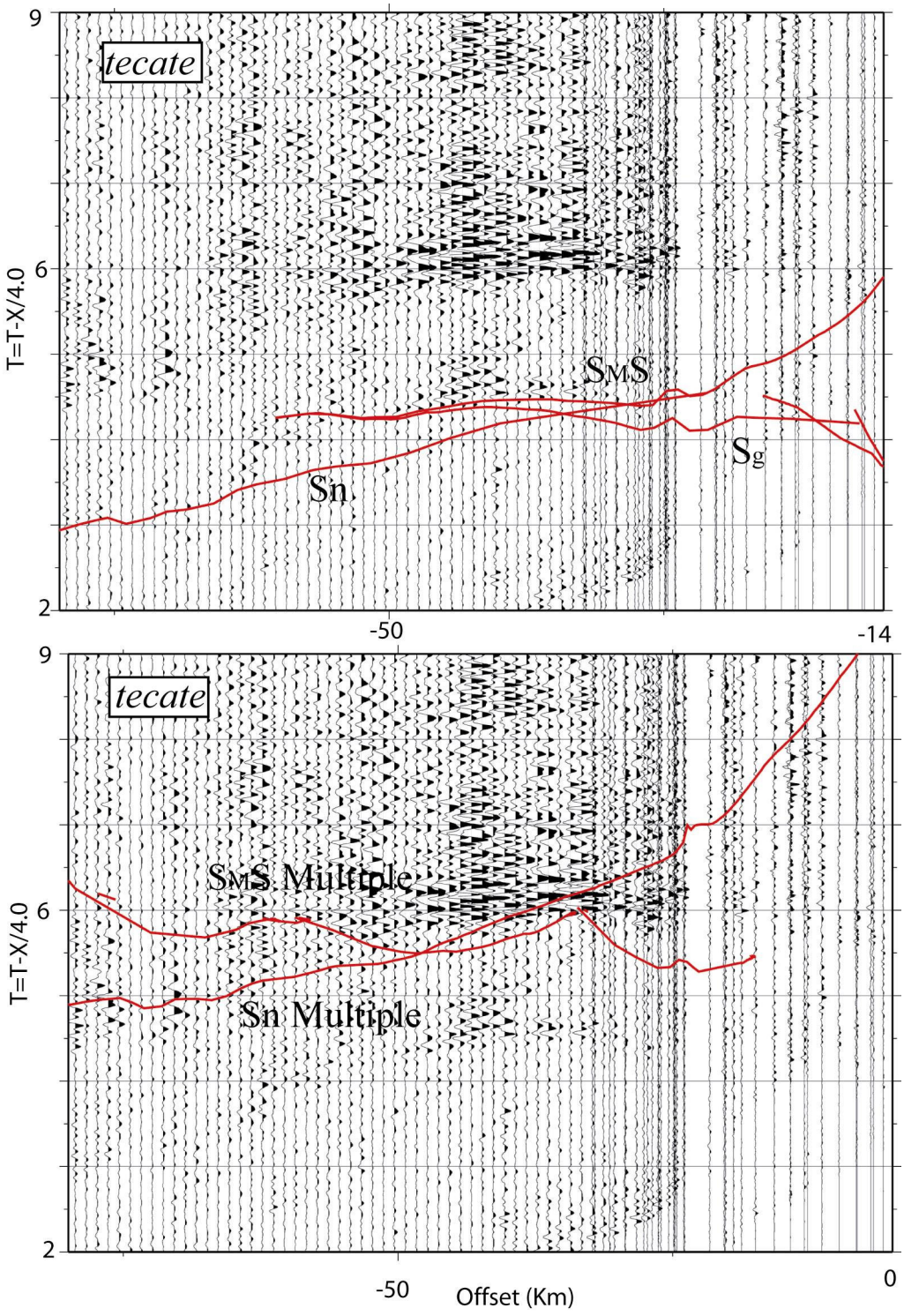

Figure 3.6 Top panel shows primary mode-converted S-waves and triplications on *tecate* whereas bottom panel shows multiples of these arrivals.

The mantle phase, S_n, is very weak at far offset, however, resulting in large uncertainty in our estimates of upper-mantle Poisson's ratio beneath Line 1. Instruments *bud* and *pete* were deployed at the end of Line 2, which is perpendicular to Line 1, and recorded coherent S_n phases reverberated in the crust along with crustal phases of relatively good quality. The S_n phases recorded on these instruments are strong enough to be identified even at far offsets (~100 km) and consequently are very helpful in assessing models having different mantle Poisson's ratios below Line 2 (Figures. 3.7 and 3.8).

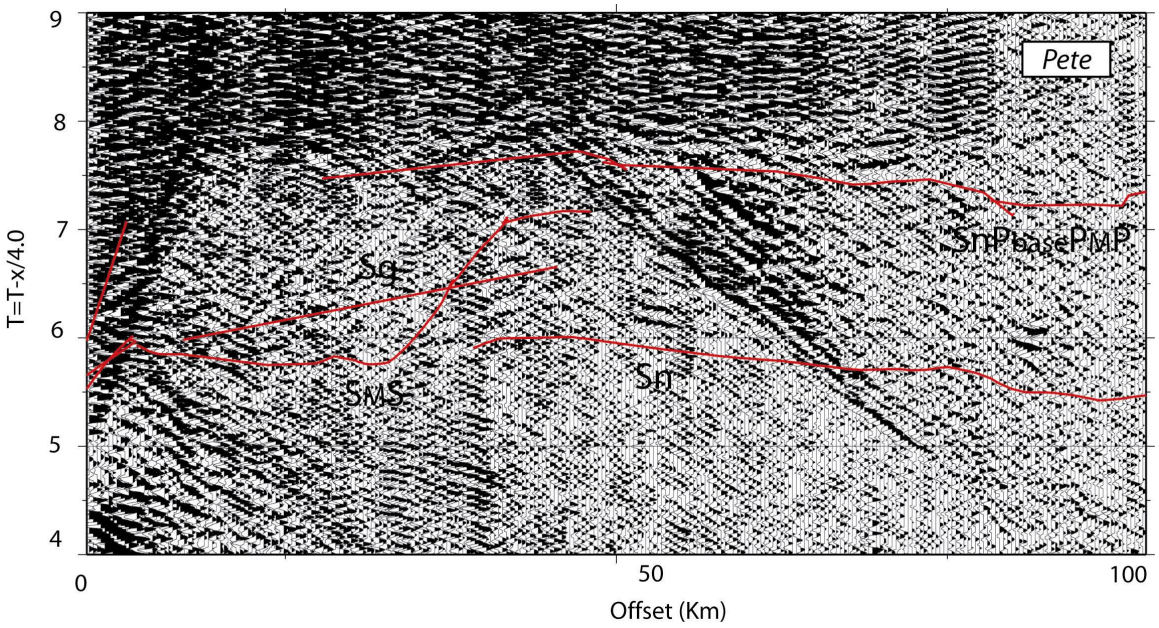

Figure 3.7 Mode-converted S-wave arrivals on *pete*.

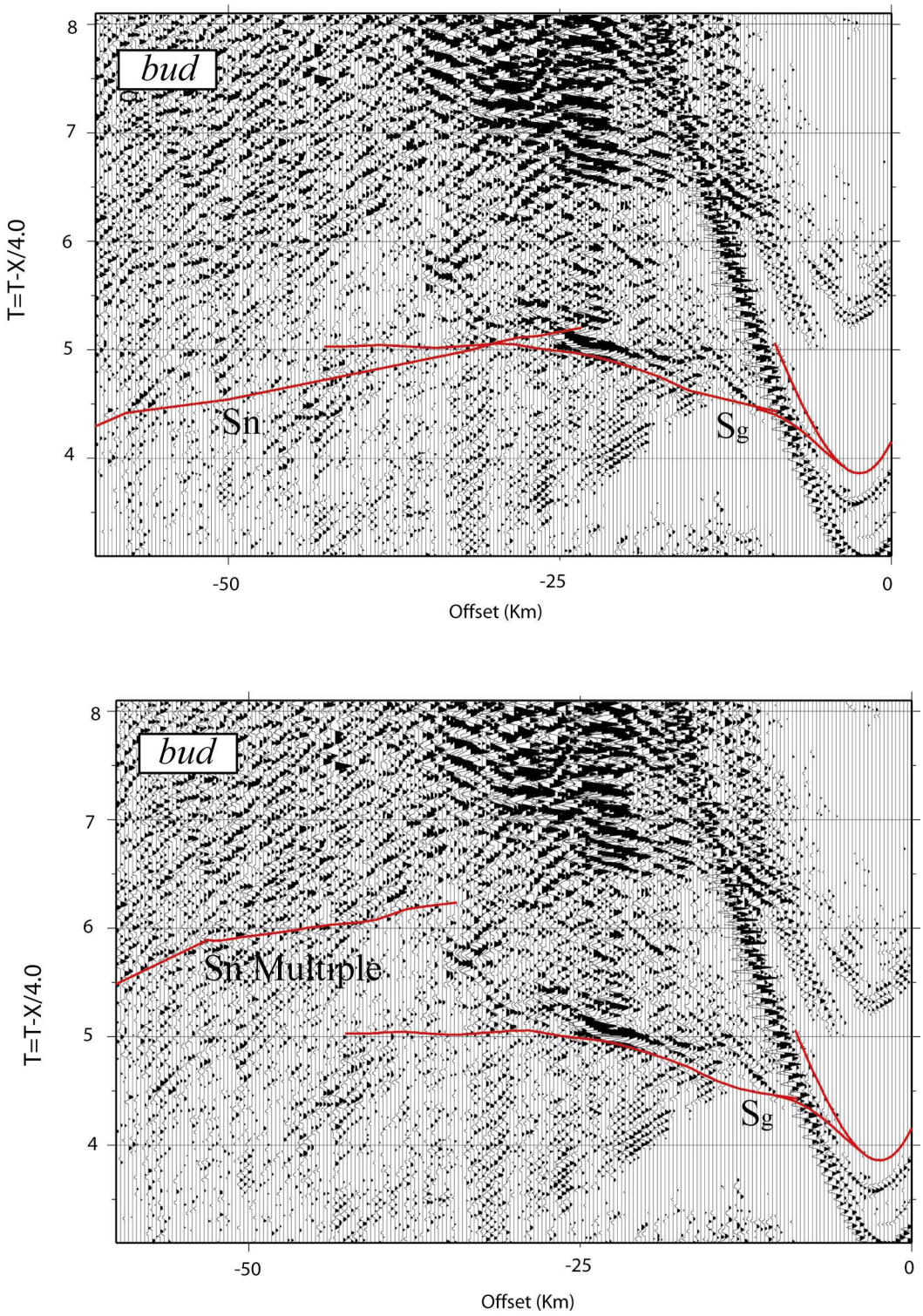

Figure 3.8 Mode-converted S-wave arrivals on *bud*. Bottom panel shows S_n that multiply reflected within oceanic crust.

The observation of P-S-P converted phases varies considerably along Line 1. As described above, there are a number of factors that control the strength of P-S conversion. The sediment/basement interface is the likely P-S conversion point in oceanic settings, including the FAIM transects. Unconsolidated, low-σ sediments favor P-S conversion at the sediment/basement interface, low-σ upper-basement rocks tend to diminish P-S conversion, and a very rough basement is likely to produce incoherent converted phases. These factors vary along Line 1, and this variation can be associated with the variable observation of converted phases along the line. However, it is difficult to say much about the variability in converted-phase observation because of the apparently trumping influence of conversion back to P near the instrument. For example, the two instruments *420* and *harp* were both located over smooth seafloor and basement. Mode-converted S-waves are observed on *420* but not on the *harp* record section. At the location of the instrument *abita*, highly incoherent S-waves are observed from shots on one side of the instrument but not from the other. No visible S-wave phases were recorded by the instrument *cass*, even though it was located between *abita* and the *tecate/carib* pair, which recorded strong mode-converted crustal phases. These observations suggest that the presence or absence of converted phases on the FAIM OBS profiles is largely dictated by the efficiency of S-to-P conversion near individual instruments.

3.3 Results

The P-wave velocity models described in Chapter 2 were used to create S-wave velocity models (Poisson's ratio models) for the relevant instrument locations of each

line, and these initial models were refined using the ray-trace forward modeling scheme of *Zelt and Smith* [1992]. The modeling steps consisted of (1) picking first arrivals of mode-converted S-waves and assigning them to appropriate classifications such as S_g, S_MS, and S_n on seismic profiles of instrument *420*, *carib*, *tecate*, *bud*, and *pete*; (2) constructing a starting S-wave velocity model by using constant Poisson's ratios for each layer in the two-dimensional P-wave velocity models; (3) conducting ray-tracing to fit primary crustal phases under the assumption that P-S conversion for down going waves or S-P conversion for up going waves takes place at the sediment/basement boundary and/or Layer-2/Layer-3 boundary; (4) with Poisson's ratios providing good fit for crustal arrivals at step 3, modeling multiply converted and reflected phases within the sediments and crust to check the model for compatibility with these other phases; (5) adding nodes to introduce lateral variability in crustal Poisson's ratios and tracing rays for the new model, which may be retained only if the travel-time fit is enhanced appreciably; (6) constraining mantle Poisson's ratios, using the crustal Poisson's ratio model, by modeling S_n phases of various order of multiplicity in reflection and conversion; (7) repeating step 2 through 6 as necessary.

For a starting model for each instrument location, it was assumed that sedimentary Poisson's ratio is in the range of 0.39-0.48, with an average values of ~0.45 along Line 1. In most cases, the value of Poisson's ratio in the sediments is not important because P-S-P phases, with conversion at the basement, travel through the sediments as P-waves. In Figure 3.2, we illustrate several paths and conversion points leading to P-S-P type converted phases observed on the FAIM OBSs. Again, because the instruments used in

this experiment had only a single, vertical-component seismometer, the recorded phases all had a conversion to P somewhere near the instrument.

For instrument *420,* we picked and modeled primary and doubly reflected S_g and S_MS within the crust, i.e. PS_gP, $PS_gP_{base}P_{seaf}P_{base}P$, PS_MSP, and $PS_MP_{base}P_MP$ (Figures. 3.3 and 3.4). Within the offset range of ~75 km, both the primary and multiple crustal phases were traced and are satisfactorily predicted with upper- and lower-crustal Poisson's ratios of ~0.30 and ~0.27, respectively. Upper-crustal Poisson's ratio at instrument *420* is not constrained by refracted S-waves through Layer 2, however, because of the very complicated pattern of the arrivals at offsets <20 km. The upper-crustal Poisson's ratio of ~0.30 was chosen such that both S_g and S_MS were satisfactorily fit. To determine uncertainties for our Poisson's ratio estimates, we followed several steps; 1) for a particular phase (S_g, S_MS, S_n, and their multiply reflected phases), we conduct ray tracing with a given Poisson's ratio in a layer, 2) we calculate the root-mean square (rms) error of misfit between travel-time predictions and picked data, 3) we perturb the Poisson's ratio until we observe a significant deterioration of fit, which is defined as having rms errors of ~0.1s or more for Line 1 phases and ~0.06-0.08s or more for Line 2 phases. The criteria are different from those used in the P-wave velocity model assessment in Chapter 2 because the quality (signal-to-noise ratio and coherency) of the mode-converted phases are not as good as the P-wave arrivals, and there are ambiguities in picking these arrivals at large offsets. In the assessment, we also consider the fact that the quality of data recorded on the instruments along Line 2 is better than along Line 1. The uncertainties of Poisson's ratios are shown in the Table 3.1 for each instrument location. As is indicated

in this table, at the location of instrument *420*, we obtained uncertainties of ~0.02 in our crustal Poisson's ratios estimates.

Table 3.1 Travel-time phases, estimated Poisson's ratio, and estimated uncertainties at each instrument location along Line 1 and 2. *Arrivals we identified and picked are both primary mode-converted phases of types indicated here and multiply-reflected variants of same kinds.

Instrument	*420 (Line 1)*	*Tecate (Line 1)*	*Carib (Line 1)*	*Bud (Line 2)*	*Pete (Line 2)*
Layer2/Layer3 Poisson's ratios	0.30/0.27	0.29/0.27	0.29/0.27	0.30/0.27	0.30/0.27
Mantle Poisson's ratios	NA	0.27	NA	0.27	0.27
*Picked phases	S_g, S_MS	S_g, S_MS, S_n	S_g, S_MS, S_n	S_g, S_MS, S_n	S_g, S_MS, S_n
Uncertainty in crustal Poisson's ratios	0.02	0.02	0.02	0.01	0.01
Uncertainty in mantle Poisson's ratios	NA	0.02	NA	0.01	0.01

For instruments *tecate* and *carib*, the well expressed primary S_g-S_MS-S_n triplications were modeled, yielding a lower-crustal Poisson's ratio of ~0.27. The record sections of both instruments also display water column multiples of this triplication, making it possible to use them as additional constraints (Figures. 3.5 and 3.6). While mantle phases are visible on both profiles (Figures. 3.5 and 3.6), they are very weak on *carib* and incoherent at far offsets on *tecate*. These phases provide the sole estimate of upper-mantle Poisson's ratio along Line 1, 0.27±0.02, and this estimate has large uncertainties because of the poor quality of the phases (Table 3.1).

For instruments *bud* and *pete*, situated at the ends of Line 2 (Figures. 3.7 and 3.8), converted crustal phases are stronger and coherent, enabling us to constrain lower-crustal Poisson's ratio of ~0.27 with an uncertainty of ~0.01 (Table 3.1). Primary and multiple mode-converted mantle phases are identified over an offset range of ~75 km and ~100 km on the profiles of *bud* and *pete*, respectively. Results of modeling these phases indicate the Poisson's ratio in the upper mantle along Line 2 is ~0.27 ± 0.01, suggesting that SV anisotropy at the FAIM site is weak. We calculate SV anisotropy as $200(V_{max}-V_{min})(V_{max}+V_{min})^{-1}$), which gives 3.5±1.7% anisotropy. These results suggest that SV anisotropy is similar to P-wave anisotropy (3.4±0.3 %) as determined by [*Gaherty et al,* 2004] in the study area.

For multiply converted waves, the location of the conversion points, either close to the shot (source multiples) or close to the receiver (receiver multiples), affects the resulting mode-converted waves in different ways [*Christesen et al,* 1997] and has implications for traveltime analyses and parameter uncertainty. P-S-P phases converted or multiply reflected near a shot generally experience more lateral variation upon multiple reflection than phases that undergo multiple reflection with conversion near the receiver. More problematic are the limitations of the traveltime modeling code [*Zelt and Smith,* 1992], which can only predict traveltimes for source multiples. We thus model receiver multiples as if they were source multiples, but, as noted, these phases may be substantially different. It is therefore difficult to distinguish misfit due to model error from misfit due to actual source- versus receiver-multiple differences, and this modeling uncertainty translates directly into parameter uncertainty. *Christeson et al.* [1997], who also used the *Zelt and Smith* [1992] inversion code and WKBJ synthetics, demonstrated

that different types of mode-converted arrivals that underwent conversion beneath receivers and shots for many instruments could not be fit satisfactorily at the same time. In reality, it is not straightforward to distinguish source multiples from receiver multiples in record sections, and so even if they could be modeled independently, it is likely that picking uncertainties would be nearly as large as the modeling uncertainty.

3.4 Discussion

Along both Line 1 and Line 2, the picked mode-converted phases are satisfactorily predicted by models with an upper-crustal Poisson's ration of 0.30, with uncertainties of ±0.02 for Line 1 and ±0.01 for Line 2, and a uniform lower-crustal Poisson's ratio of ~0.27, with uncertainty of ±0.02 and ±0.01 for Line 1 and 2, respectively. The estimated upper-crustal Poisson's ratios are typical of old oceanic crust (> 60 Ma) consisting of basaltic rocks [*Shaw,* 1994; *Christeson et al,* 1997; *Collier and Singh,* 1998], consistent with seafloor age in this area. As we describe below, Poisson's ratio values in the range estimated for the lower crust (0.27±0.02), in combination with a lower-crustal V_P of ~6.7 km/s, are more consistent with a gabbroic lower crust than a lower crust that contains substantial serpentinite. Similarly, with an upper mantle V_p of 8.0-8.2 km/s, the estimated mantle Poisson's ratio (~0.27 ±0.01/0.02) also agrees with laboratory measurements of the unaltered peridotites that are presumably constituents of the upper-mantle.

The Poisson's ratio within Layer 2 (0.30±0.01/0.02) may be a natural consequence of the old age of oceanic crust in the study area. Low upper-crustal Poisson's ratios (σ as low as 0.24) have been observed within Layer 2 at depths of 0.8-2.0 km on young

oceanic crust [*Spudich and Orcutt,* 1980; *Au and Clowes,* 1984]. Since laboratory measurements of unfractured basalts, diabases, and gabbros have Poisson's ratios of 0.28-0.30 [*Christensen,* 1996], these low Poisson's ratios must be indicative of either anomalous composition or high porosity in this depth interval. Several explanations have been offered to explain these low Poisson's ratios. *Spudich and Orcutt* [1980] proposed that quartz rich rocks (quartz has low Poisson's ratio of ~0.22) might be located in the shallower part of the Layer 2; *Shearer* [1985] suggested that thick cracks embedded in the basaltic rocks might cause lower Poisson's ratios; and *Fryer et al.* [1989] argued that anisotropy created by horizontal fractures could be responsible for the lower Poisson's ratios. It seems, however, that the model proposed by *Shaw* [1994] may provide the most plausible account for age-dependent Poisson's ratios in the upper crust. *Shaw* [1994] pointed out that all observations of low Poisson's ratio occur on young oceanic crust and proposed a model in which thin and thick crack populations vary with depth. As mentioned in the section 3.1, in this model, thin cracks are sealed in young upper crust, but thick cracks remain open, thus producing a low Poisson's ratio at depth. According to this model, in older crust, both crack populations are sealed, restoring Poisson's ratio to laboratory values. Therefore, the constrained upper crustal Poisson's ratios in this study are consistent with assessments of *Shaw* [1994] and *Christeson et al.* [1997].

Relationships between Poisson's ratio and lithology have been used to constrain the composition of continental and oceanic lithosphere [e.g. *Ludwig et al,* 1970; *Zandt and Ammon,* 1995; *Christensen,* 1996; *Brocher,* 2005]. For volcanic rocks, Poisson's ratio is highly variable because of many factors that also produce wide ranges in velocities in these rocks. Alteration may be common, and many of the alteration products have quite

different elastic properties than the parent rocks. Porosity is usually high in volcanic rocks, and a significant proportion of porosity is often in the form of small vesicles, which are not closed with hydrostatic pressure. Glass may also be a common constituent of many volcanic rocks, thus influencing V_s.

Unlike extrusive rocks, there is a clear trend relating Poisson's ratio with composition for common plutonic rocks. The relatively low Poisson's ratio of granitic rocks, ~0.24, increases to 0.27 as the mineralogy changes to that of diorite, and the transition from diorite and gabbro is marked by a further increase in Poisson's ratio to 0.295 [*Christensen,* 1996]. The low Poisson's ratio of granites is in agreement with mineralogy and can be attributed to the significant quartz content of granites. The transition from granitic to gabbroic composition is accompanied by decreasing modal quartz and an increase in the anorthite (calcium end-member of plagioclase) content of plagioclase feldspar, both of which increase Poisson's ratio [*Christensen,* 1996; *Brocher,* 2005]. Many mafic and ultramafic igneous intrusions, which may be representative of mantle lithology, contain gabbro and peridotite or dunite that have originated from magmatic differentiation. A gradual change from gabbro to olivine-rich gabbro and dunite lowers Poisson's ratio to approximately 0.26 while increasing V_P to 8.4 km/s. This decrease in Poisson's ratios is due primarily to decreasing amounts of plagioclase feldspar and increasing olivine content [*Christensen,* 1996]. As dunite (σ=0.25) is hydrated to serpentinite, there is a progressive change in Poisson's ratios to 0.36, and partially serpentinized dunites and peridotites have Poisson's ratios that fall between these values, i.e. σ=0.25-0.36 [*Christensen,* 1996; *Brocher,* 2005]. Average Poisson's ratios for a variety of mafic rocks show major changes with increasing metamorphic

grade. Initially high Poisson's ratios of low-grade mafic rocks (~0.29) decrease significantly to 0.26 for green-schist and amphibolite facies rocks. The transition to the granulite faces is accompanied by an increase in Poisson's ratio to 0.28 followed by a slight decrease to 0.27 as ecologite faces assemblages become stable [*Christensen,* 1996].

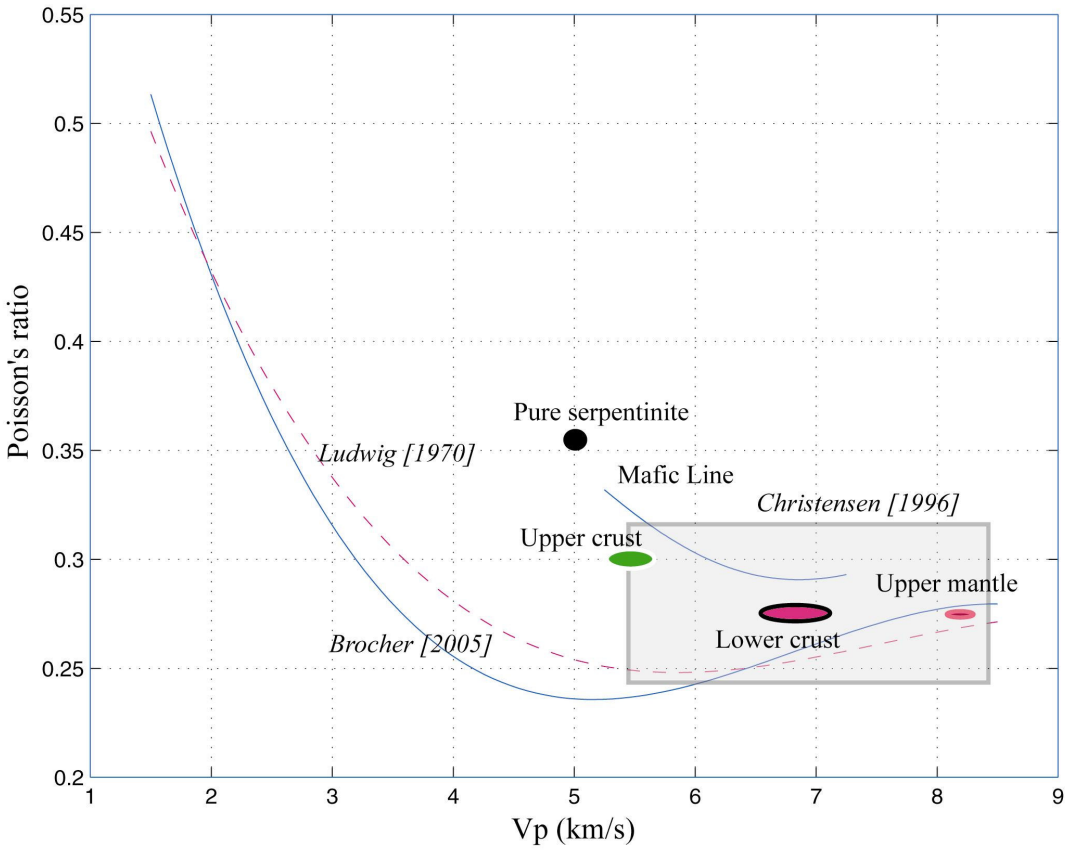

Figure 3.9 Constrained Poisson's ratios (ellipsoids) plotted with regression curve of *Brocher*, [2005], *Ludbig*, [1970], and Mafic line (*Brocher*, [2005]). The shaded box denote range of Poisson's ratios of plutonic rocks (*Christensen*, [1996]).

We use empirical relationships between Poisson's ratio and V_P for various lithologies to infer crustal lithologies for the FAIM transect based on the results we have described here. In Figure 3.9, we indicate a boxed region in σ-V_P space that *Christesen* [1996] defines as the range of Poisson's ratio related to mineralogical changes (by metamorphism and alteration) in mafic rocks. The solid red and green broken curves are regressions of σ onto V_P from *Brocher* [2005] and *Ludwig* [1970], and the blue solid curve is the σ-V_P regression from *Brocher* [2005] for mafic and calcium-rich rocks, which he calls the "mafic line". The ellipsoids represent the crustal and mantle Poisson's ratios estimated in this study. The FAIM lower crustal Poisson's ratio estimate (0.27 ± 0.01) plots near the lowermost segment of the "mafic line", suggesting that the lower crust is likely to consist primarily of mafic igneous rocks (gabbroic rocks) rather than partially serpentinized mantle rocks (peridotites or dunites). This value of lower crustal Poisson's ratio occupies the middle of the box of *Christesen* [1996], further supporting the inference that lower crust beneath the FAIM transects is not significantly affected by serpentinization. Both V_P and Poisson's ratio of the upper-mantle are typical of mantle rocks and can be predicted by the regression curves of *Brocher* [2005] and *Ludwig* [1970]. The combined observations of 1) a seismically sharp crust/mantle boundary, 2) Layer-3 Poisson's ratio and V_P values characteristic of gabbroic rocks, and 4) upper-mantle V_P characteristic of peridotitic rocks together provide strong support for the notion that the crust (i.e. material above the seismic Moho) beneath the FAIM transects consists mostly of melt-derived igneous rocks as opposed to consisting of a significant amount of serpentinized mantle rocks. This result thus tends to support the

inferences based on velocity structure and gravity modeling that variations in crustal thickness, upper mantle velocity gradient, and density along FAIM Line 1 are due to melt retention.

The results of modeling S_n phases, though flawed by a low signal-to-noise ratio and incoherence along Line 1, indicate that measured upper-mantle Poisson's ratio is ~0.27±0.02 and 0.27±0.01 below Line 1 and Line 2, respectively. This uniform Poisson's ratio (~0.27) in the upper-mantle, with uncertainties, translates into 3.5±1.7% anisotropy in V_S. These amounts of S-wave anisotropy are similar to the measured P-wave anisotropy of 3.4±0.3% [*Gaherty et al,* 2004], which is approximately 50% of that found in lithosphere formed at faster spreading rates in the Pacific. Near the Nootka fault zone off the west coast of Canada, *Au and Clowes* [1984] obtained non-uniform Poisson's ratios in the upper-mantle of 0.22 (V_s = 4.5 km/s) and 0.28 (V_s = 4.6 km/s) in directions approximately parallel to the spreading ridge and parallel to direction of spreading, respectively. This prominent anisotropy in Poisson's ratios corresponds to low S-wave anisotropy that contrasts sharply with the 10% P-wave anisotropy in the same area. In this study, constrained Poisson's ratios with weak P- and S-wave anisotropy could be ascribed to a consequence of enhanced brittle deformation in the upper-mantle due to more pervasive conductive cooling during slow spreading [*Gaherty et al,* 2004]. This process in turn could inhibit high degrees of shear deformation, which induces a lattice-preferred orientation of olivine crystals responsible for seismic anisotropy.

3.5 Conclusions

In this chapter, we have presented results of modeling mode-converted P-S-P type waves recorded on the vertical component of instruments *420*, *carib*, *tecate* along Line 1 and *bud* and *pete* deployed at the end of Line 2. We identified and picked S_g, S_MS, S_n, and their multiply reflected variants. Ray-trace forward modeling was conducted based on previously obtained P-wave velocity models with assigned Poisson's ratios in each layer. We constrained lower crustal Poisson's ratios of 0.27±0.02/0.01 (Line 1/Line2) which, based on laboratory measurements of Poisson's ratio and V_P on known lithologies [*Chritensen,* 1996; *Broucher,* 2005] and supported by an observed seismically sharp crust/mantle boundary, suggests that the lower crust consists primarily of melt derived igneous rock with negligible serpentinite. These results thus support the notion that changes in crustal thickness reflect changes in mid-ocean ridge crustal production processes. We constrained upper-mantle Poisson's ratios of ~0.27 along both Line 1 (±0.02) and 2 (±0.01), suggesting that the SV anisotropy in this area is weak, similarly to previously measured P-wave anisotropy. Therefore, our results also reinforce inferences on ductile shear deformation based on P-wave studies.

CHAPTER 4

INFERENCES ABOUT UPPER MANTLE STRUCTURE BASED ON GEOID VERSUS TOPOGRAPHY RATIOS

4.1 Introduction

In Chapter 2, we showed that a change in crustal thickness of ~1.5 km occurs along FAIM Line 1, and that this change correlates with a spreading-rate change. In particular, a ~1.5 km decrease in crustal thickness occurred as spreading rate decreased from ~13 mm/yr (half rate) to < 10 mm/yr at ~132 Ma. This observation is consistent with a handful of crustal thickness measurements from ultra-slow spreading lithosphere in other locations. The widely held explanation for these observations has been that slower spreading leads to decreased mantle melting due to the influence of a thicker thermal lid [e.g. *White et al.*, 2001]. However, we also show in Chapter 2 that a density model based on this explanation does not predict the observed gravity. In order to satisfy the crustal thickness constraints and observed gravity anomalies, the density of the mantle underlying the thinner crust needs to be reduced. It turns out that if the mantle density beneath the thinner crust is reduced by an amount equivalent to the addition of ~1.5 km of crustal-density material to the mantle distributed over 30 – 80 km, then the crustal-thickness and gravity observations are explained and the resulting density structure is in isostatic equilibrium. This mantle structure contains a lateral transition across the location of the spreading-rate change, and precisely such a transition is required to explain observations of mantle P-wave refractions along the FAIM transect [*Lizarralde et al., 2004*]. These results led *Lizarralde et al.* [2004] to propose that melt extraction, rather than melt production, is the process most sensitive to spreading-rate change at slow

spreading rates, and that the low-density material underlying the thinner crust beneath the eastern portion of the FAIM transect corresponds to gabbroic inclusions that were trapped beneath the spreading center during lithospheric formation.

The change from slow to ultra-slow spreading along the FAIM transect is not a local phenomena. It occurred along many hundreds of kilometers of the mid-Atlantic ridge, as documented by magnetic anomalies [*Klitgord and Schouten*, 1986], corresponding plate-age and spreading-rate compilations [*Müller et al.*, 1997], and evidenced by a regional rough/smooth basement-topography boundary [*Sundivik et al.,* 1984]. We would expect, then, that the transitions in crustal and upper-mantle structure observed along FAIM Line 1 should also be observed at the location of the spreading-rate change along other transects that cross this spreading-rate transition. This is a basic prediction of our melt-retention hypothesis. In this chapter, we endeavor to assess this prediction, and so test our hypothesis, by analyzing geoid/topography ratios along regional transects.

A competing hypothesis to explain the FAIM observations invokes decreased crustal production at slower spreading rates to explain the crustal-thickness observations, followed by a perturbation to upper-mantle structure related to processes that caused the Bermuda magmatism and formed the Bermuda swell at around 40 Ma [*Detrick and Crough*, 1978]. A melt-retention mechanism would predict similar transitions in mantle properties south of the FAIM transect and a possible obscuring of this transition northward, as the onset of the later Bermuda event obscures this structure. A "Bermuda" mechanism explains the transition in mantle properties as thermal or melt-related perturbations centered at Bermuda that only coincidentally correlate with the spreading-rate change along the FAIM transect. This mechanism would predict a lateral transition

in mantle properties that, south of the FAIM transect, decreases with distance from Bermuda and progressively de-correlates with the regional spreading-rate change since the perturbation from Bermuda presumably extends radially outward. North of the FAIM transect, one might expect a Bermuda mechanism to lead to a strengthening of the lateral transition in mantle properties.

In this chapter, we employ a novel analysis of geoid/topography ratios to make inferences about mantle structure in the region near the FAIM transect. In addition to testing hypotheses on the origin of structure observed along the FAIM transect, a principle objective of this work is to explore the usefulness of forward geoid calculations in assessing mantle structure. In the absence of seismic observations, potential fields provide the only available data to make these inferences. Gravity anomalies are not well suited to this task, however, since their resolution decreases with depth, and they are thus strongly biased by crustal structure. The geoid, however, represents, to first order, a depth-weighted integral of density perturbations, and so should possess sensitivity to relatively sharp lateral transitions in density perturbations that extend well into the mantle. We find that geoid/topography ratios are sensitive to the depth extent of density perturbations. The model with shallowest depth extent consistent with the gravity data (30 km) explains observed geoid/topography ratios along the FAIM transect and the misfit increases as the mass distribution depth increases, reinforcing the conclusion of Chapter 2. We also show that there are correlations between geoid/topography ratios and the spreading-rate transition up to ~150 km south of FAIM Line 1. The best-fitting lithospheric density model for the FAIM transect does a good job at predicting the

geoid/topography ratios along tracks within ~100 km south of FAIM Line1, suggesting that there is a common explanation for these observations.

4.2 Satellite measurements

In this section we briefly review satellite altimetry, bathymetry derived from these data, and how geoid/topography ratios can be used to study lithospheric mass distribution and isostasy. Altimetry data over the ocean can be obtained by both active and passive sensing. Passive sensing employs perturbations in satellite orbital paths due to the non-sphericity of Earth's gravity field to infer the shape of equipotential surfaces. If Earth were a homogeneous sphere, then an orbiting satellite would follow an elliptical path that does not change with time.

Earth, however, is neither spherical nor uniform in density, and a satellite thus experiences torques that cause its orbit to precess so that the intersection of its orbital plane with Earth's equatorial plane varies with time, a phenomenon known as nodal regression. This precession provides a means of determining the shape of the geoid and gravity anomalies via passive sensing.

In this study we use data derived from active sensing. During the SKYLAB mission in the 1970's [*Haxby and Turcotte*, 1978], sea-surface heights were measured employing an earthward-directed microwave (13.9 GHz) pulse with a precision of a few meters. These measurements were followed by radar altimeter missions such as GEOS-3, SEASAT, GEOSAT, ERS-1, and TOPEX/POSEIDON. Figure 4.1 shows how radar altimetry is carried out in practice. Let's assume that the altitude of the satellite with

respect to sea surface is known, then the height of the geoid relative to the reference ellipsoid, *N*, is given by

$$N=h-h_s=H_1-H_2-h_s \tag{4.1}$$

where *h* is the height of the sea surface above the reference ellipsoid, h_s is the separation of sea level and the geoid, H_1 is the height of the satellite altimeter above the reference ellipsoid, and H_2 is the height of the satellite above the sea surface [*Jones,* 1999].

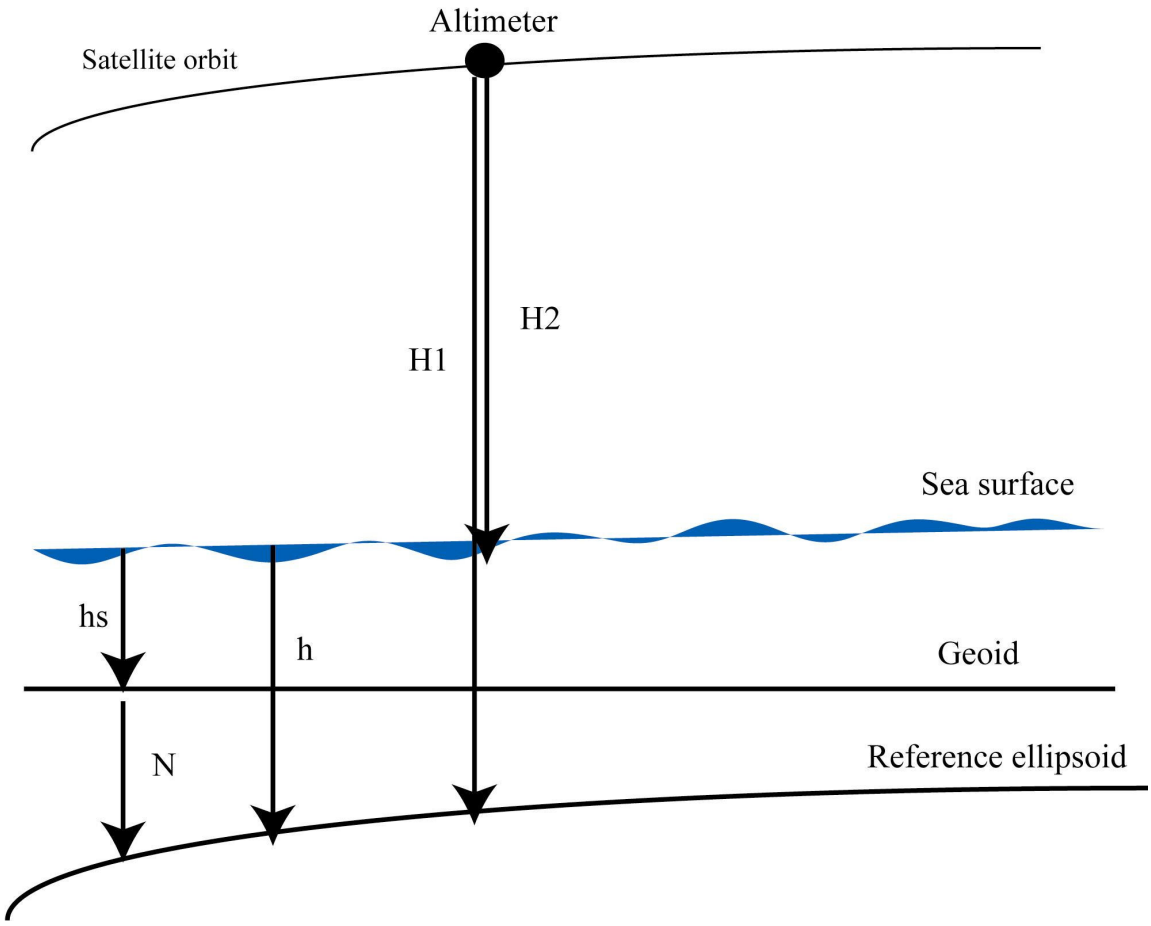

Figure 4.1 This figure illustrates principles of satellite altimetry.

The parameter h_s is known as the sea surface topography, which is varies with oceanographic and meteorological effects including tidal changes, ocean currents, wind stress, and variations in water density. These variations are usually two orders of

magnitude less than height variations in the geoid and can be reduced by taking averages of H_2 [*Jones,* 1999].

In active sensing, the largest source of the error in measured geoid height arises from uncertainties in the satellite's position with respect to the reference ellipsoid. The point-to-point precision of SEASAT height measurements was less than 10 cm, each height value representing an average of observations taken during 1s when the satellite moves ~7 km along the ground track [*Jones,* 1999]. The joint US/French TOPEX/POSEIDON satellite has an instrumental precision of 2 cm and an absolute accuracy of ~10 cm [*Jones,* 1999].

Ocean floor structures with horizontal scales of a few to 10 kilometers and vertical scales of 100 m or more generate sea surface gravity anomalies observable with satellite altimeter [*Smith,* 1998]. Prior to 1990, altimeter data resolved only tectonic lineaments, seamounts, and some aspects of mid-ocean ridge structures. As new altimeter data have become available, seafloor structures of ~10-km scale have been resolved throughout the world's oceans, revealing structures associated with seafloor spreading processes including ridge jumps, propagating rifts, and variations in magma supply [*Smith,* 1998]. It has been proposed [*Small and Sandwell,* 1989; *Smith,* 1998] that the amplitudes of fine scale (10-80 km) sea-floor roughness on old oceanic lithosphere is spreading-rate dependent, as observed at present mid-ocean ridges, implying that fine-scale tectonic fabric is generated primarily by mid-ocean ridge processes.

4.3 Geoid and isostatic anomalies

The geoid provides useful information on density anomalies of different origins and over various ranges in the earth. Topography of various scales can contribute to the measured potential field or gravity of the earth. In Chapter 2, we showed that very short wavelength bathymetry significantly affects gravity and the importance of having detailed bathymetric data to model marine gravity along a specific track. These topographic features with small horizontal extent (<100 km) are not necessarily in isostatic equilibrium because of the finite strength of the lithosphere. Since Earth's mantle behaves like a fluid over geologic time scales, topographic features with wavelengths in excess of few to several hundreds km are generally in isostatic equilibrium above some compensation depth. Lateral density variations above the compensation depth generate geoid anomalies that can be referred to as the "static" component of the total geoid anomaly. The geoid also has dynamic components, which are manifestations of deeper mantle convection and are expressed as longer wavelength (>1000 km) geoid undulations. Characterization of the dynamic components of the geoid requires a calculation of mantle flow in response to density anomalies [e.g. *Conrad,* 2005]. Our primary interest in this study is to characterize density anomalies within the uppermost part of the lithosphere below the area in the vicinity of the FAIM transect. We model geoid anomalies predicted for the two-dimensional density models we obtained in Chapter 2 using a formula that relates geoid height to a static density distribution. We will show that a key anomaly in the observed field is explained by the static anomaly, but that a large dynamic component is apparently also present in the observed geoid.

Ockedon and Turcotte [1978] derived a formula relating geoid anomalies to topography assuming that the horizontal scale of the density variation is large in

comparison with the vertical scale. It is generally accepted that isostasy is a good approximation over relatively large horizontal distances because Earth's mantle behaves like a fluid on a geological time scale. Hence we can assume that local density variations are in isostatic equilibrium above a depth of compensation, thus $\Sigma\Delta\rho(z)\Delta z = 0$. In this expression, $\Delta\rho(z)$ is density distribution with respect to depth z and Δz is depth interval. Consequently, the expression for the gravitational potential or geoid height in isostatically compensated regions is proportional to the first moment of the density distribution:

$$\Delta N = (-2\pi G/g)\, \Sigma z \Delta\rho(z)\Delta z\ , \qquad (4.2)$$

where G is the gravitational constant and g is the local gravitational acceleration. If one uses explicit relationships between density and depth (z), then the equation for ΔN yields specific geoid anomaly functions with topography as an independent variable.

The geoid and geoid/topography ratios have been used to characterize regional upper mantle structure, most commonly characterized in terms of regional compensation mechanisms. *Haxby and Turcotte* [1978] showed that different mechanisms of isostasy (i.e., thermal, Airy, and Pratt) correspond to different geoid versus topography relationships. For Pratt compensation, surface topography is compensated by a variable-density mass column above a constant compensation depth, whereas Airy compensation assumes a constant density above a varying compensation depth. In both cases the equations for geoid/topography ratios can be derived. Airy compensation predicts a hyperbolic relationship between the geoid anomaly and topography, and Pratt compensation predicts a linear relationship. For lateral density and topography variations resulting primarily from thermal subsidence away from mid-ocean ridges ("thermal

isostasy"), a linear geoid/topography function is predicted. These relationships are useful for saying things about regional structure based on geoid/topography ratios. A low geoid/topography ratios often indicates *Airy* compensation. A higher ratio may suggest Pratt and/or thermal isostasy and dynamic uplift from a mantle plume. A very high geoid/topography ratio, which is poorly correlated with topography may be evidence of mantle convection [*Parson and Daly,* 1983]. To study localized density anomalies, however, or to test hypothesis based on particular density structures, one may evaluate equation 4.2 directly. We adopt this direct approach here.

4.4 Results

We analyze and interpret geoid/topography ratios along the 800-km-long main transect of the FAIM experiment (Line 1 in Fig. 1.1) and tracks of the same length parallel to this line in the Western Atlantic basin. We use the National Ocean and Atmospheric Administration (NOAA) GEOID03 (Figure 4.2) geoid model, covering the conterminous United States [*Roman et al,* 2004]. There are no formal accuracy estimates for this model, but preliminary analysis [*Roman et al,* 2004] shows that geoid error is close to ±2.5 cm, with a horizontal resolution of 1 arc-minute. We use gridded bathymetry derived from satellite altimetry and ship depth sounding [*Smith and Sandwell,* 1997; *Smith,* 1998]. These data resolve tectonic details to 5-10 km in location and within 100-250 m in depth in many cases. Along the FAIM transect (Figure. 1.1), we utilize hydrosweep bathymetry data collected during the FAIM experiment aboard the R/V *Maurice Ewing* in 2001.

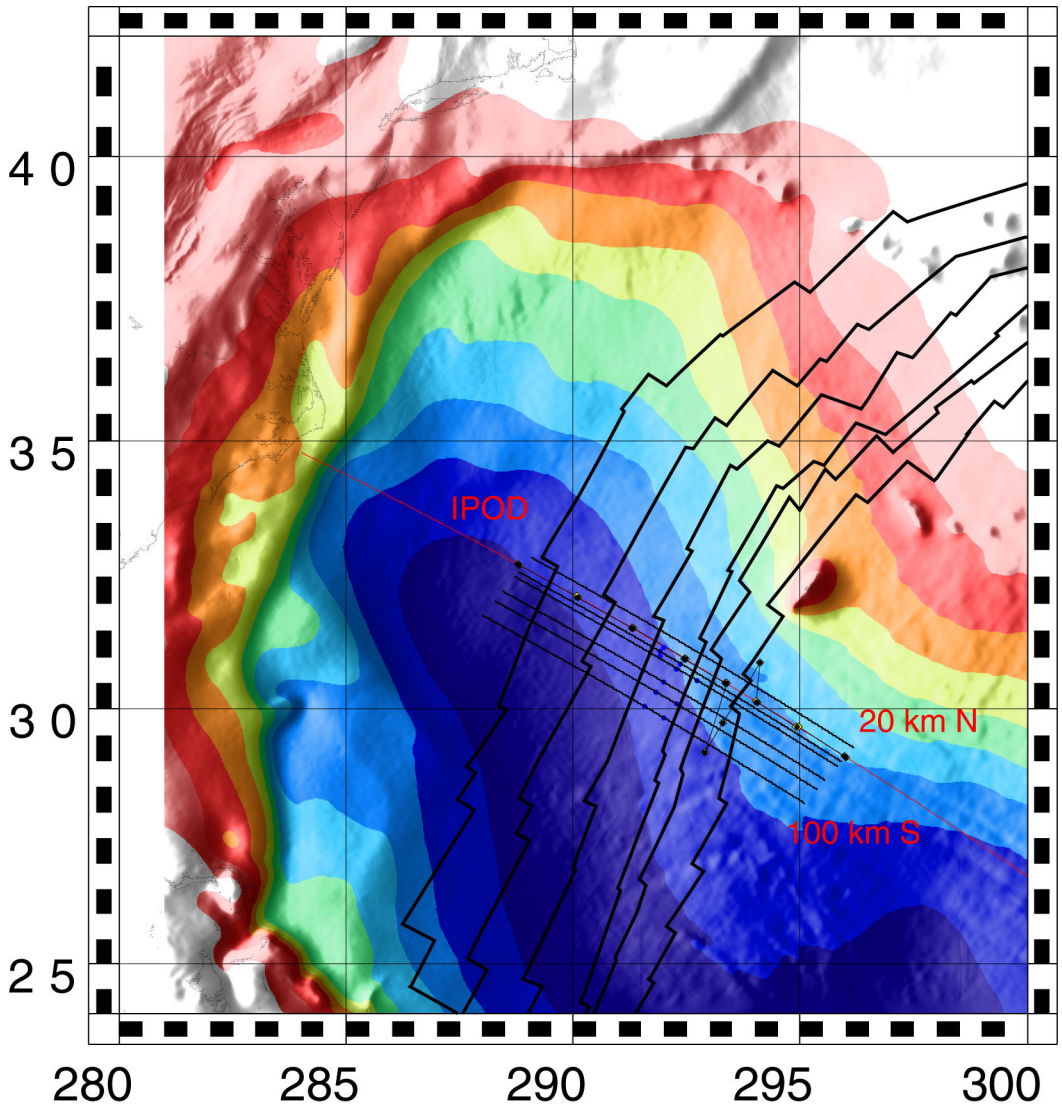

Figure 4.2 The GEOID03 image of the north Atlantic basin with several tracks along which we find out correlation between geoid versus topography ratios and changes in spreading rate.

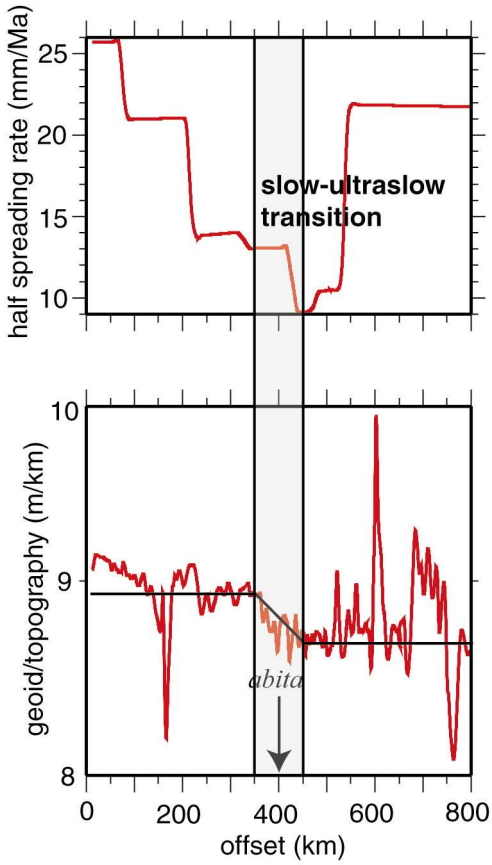

Figure 4.3 Spreading rate and geoid versus topography ratios profile along Line 1 in figure 1.1. Changes in long wavelength components of geoid/topography ratios correlate with smooth-rough seafloor boundary (approximately situated at the instrument *abita*) and slow-ultra-slow spreading transition.

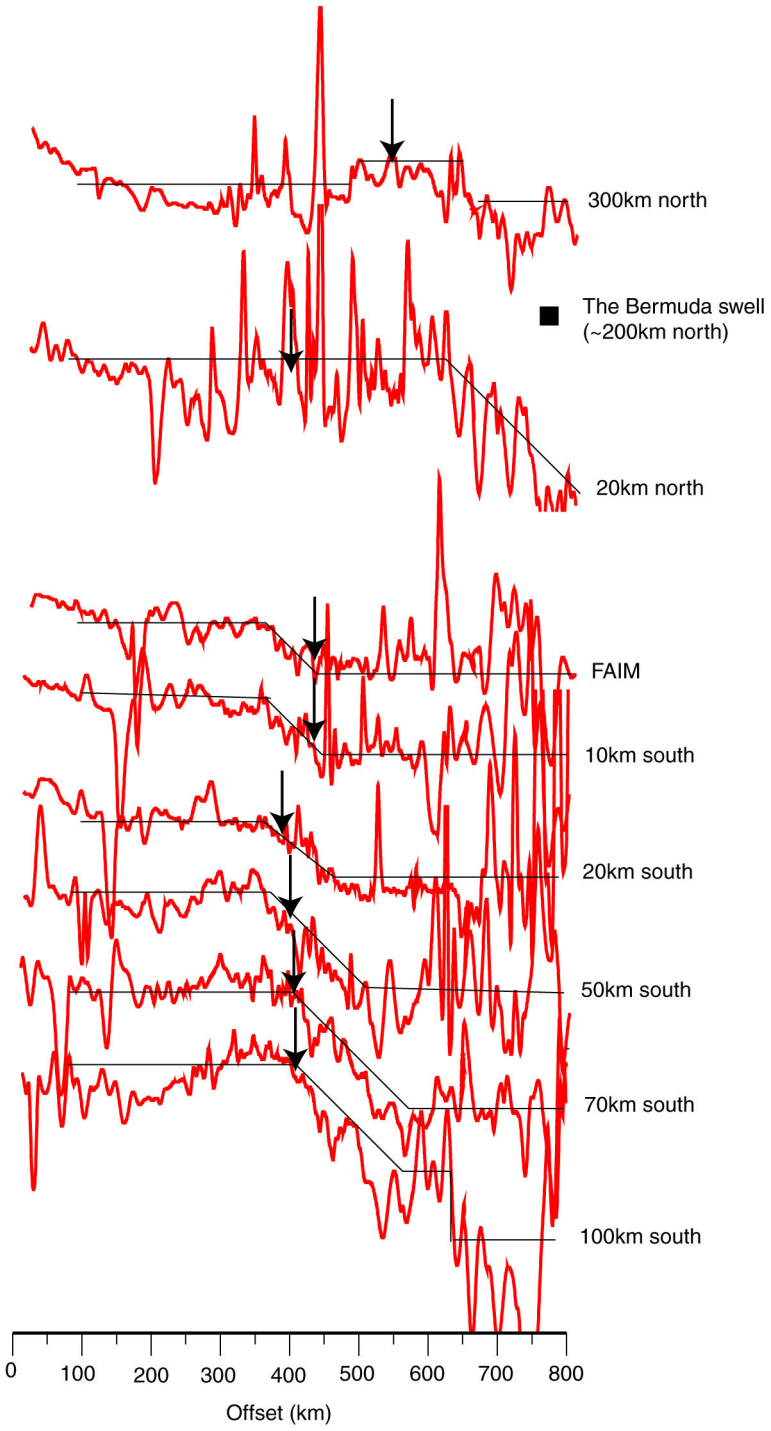

Figure 4.4 Different long wavelength patterns of geoid/topography ratio profiles in the south and north of the FAIM transect. Arrows indicate locations of slow-ultraslow spreading transition in each track. The black lines show intermediate wavelength

patterns in ratios along the files. In the north of the transect, there is no correlation between geoid/topography ratios and changes in spreading rate.

Based on these data, we calculated the geoid/topography ratios along Line1 and along tracks parallel to this transect shown in Figure 4.3 and 4.4. The geoid/topoigraphy ratios along these tracks appear to be correlated with the spreading rate change and the rough/smooth basement boundary. Figure 4.4 shows that these correlations seem to persist to ~100 km south of the FAIM transect, and that there is no obvious correlation north of the transect. These observations are consistent with the expectations described above for the melt-retention hypothesis, though the distance over which the correlation is observed to the south is quite small.

We can assess the relevance of these correlations by calculating geoid/topography ratios using the density models developed in Chapter 2. In Chapter 2, we show that density models that satisfy both observed gravity and the crustal thickness constraints require low density material distributed over 30-80 km depth below the thinner crust of the eastern half of the transect. These density models exhibit an abrupt lateral transition in vertical density gradient towards the center of the model near the location of the change from slow to ultra-slow spreading rate. We calculate the predicted geoid and geoid/topography ratios from these models employing the discrete form of the relationship between geoid height and density,

$$N(x) = (2\pi G/g) \Sigma \Delta\rho(x,z)\, z\, \Delta z . \qquad (4.3)$$

As mentioned earlier, N(x) is geoid height, G is the gravitational constant, g is the mean gravitational acceleration, which is ~9.81m/s^2, $\Delta\rho(x, z)$ is the density anomaly, and Δz is

the depth interval of our model grid. These calculations (Figure 4.5) show that the observed geoid/topography ratios along FAIM are well predicted by the density model developed in Chapter 2 based on gravity data. In Chapter 2, we found that density models with low-density material distributed over depths varying from 30 to 80 km were statistically indistinguishable. The geoid calculation shown in Figure 4.5 suggests that the model with the shallowest melt distribution (~30 km) may be the preferred model to explain both observed gravity and geoid/topography ratios along Line 1.

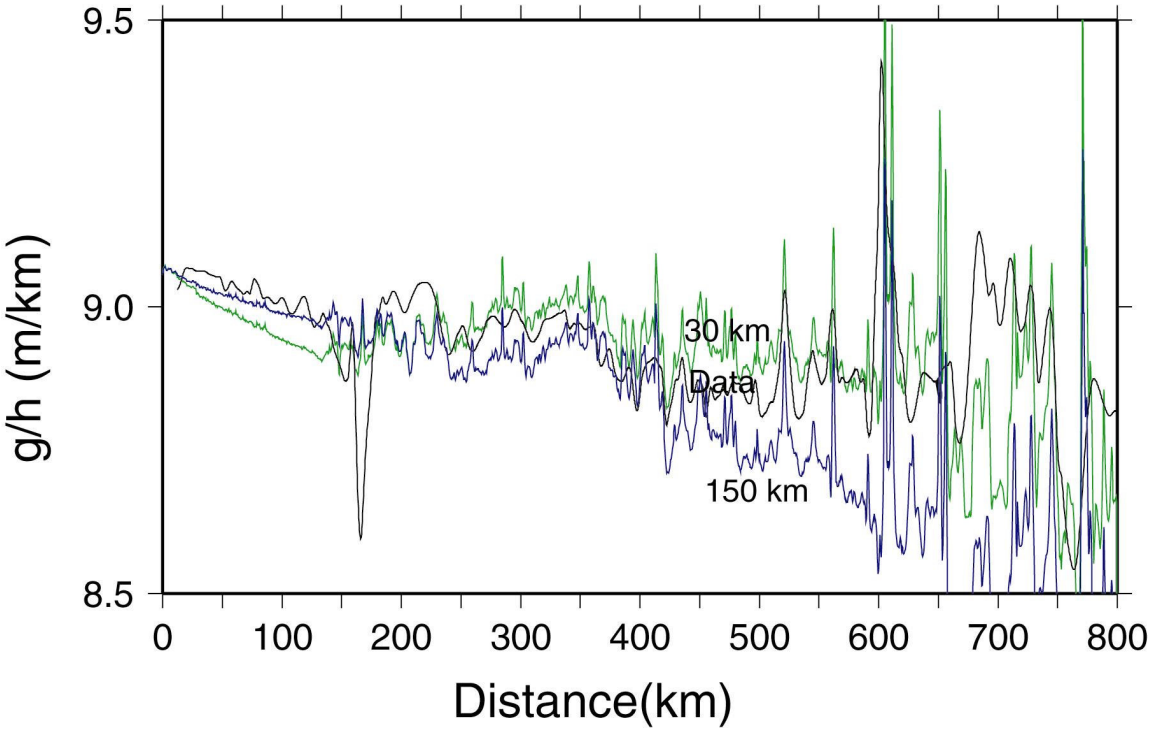

Figure 4.5 This figure shows observed geoid/topography ratios and those calculated from the models with different mass distribution depths.

Although not shown in the Figure 4.5, the "isostatic" and "seismic Moho" models described in Chapter 2 yield predicted geoid/topography ratios with relatively large misfit

with respect to the observed ratios. To determine what parameters govern the shape of the geoid/topography ratio profile in the interval in which spreading rate changes from slow to ultraslow, we also calculated geoid/topography ratios using models with simpler interfaces. In these models, we use a flat seafloor and basement, and the depth to the Moho is the only interface that varies in each model with different mass distribution depth. Results of these calculations indicate that the mass distribution depth is more important than Moho depth in controlling the height and sharpness of "*transition ramp*" seen in the observed geoid/topography ratios (Figure 4.6). The height of transition ramp unrealistically increases compared to that in the observed geoid/topography ratios as the mass distribution depth increases, resulting in appreciable misfit.

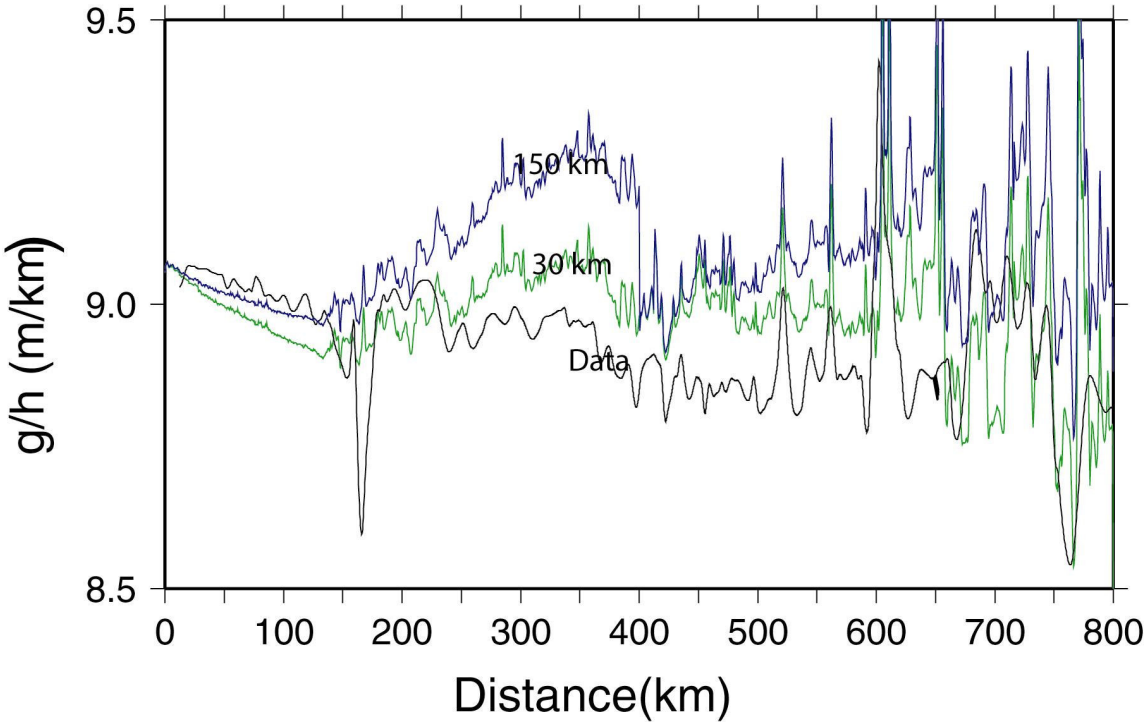

Figure 4.6 geoid/topography ratios calculated from the models having simplified interfaces with different mass distribution depth. The height of transition ramp is very sensitive to the mass distribution depth.

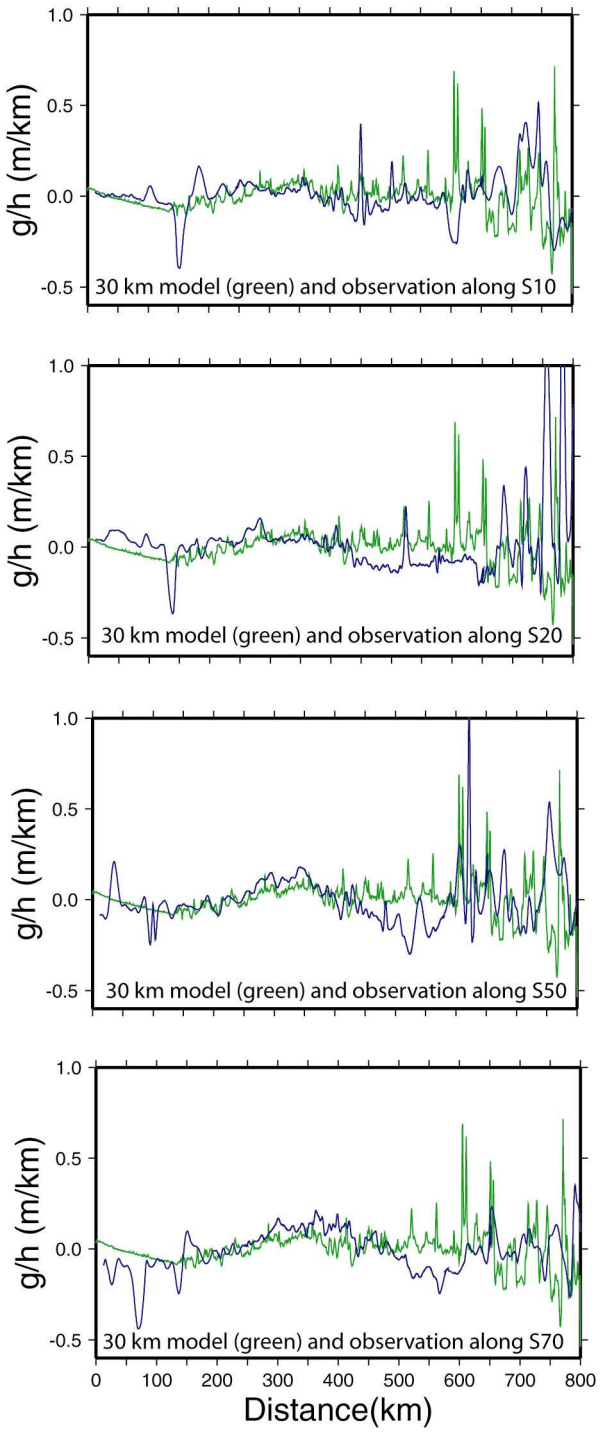

Figure 4.7 This figure shows overlay plots of geoid/topography ratios from 30 km model and observations along the tracks 10 (S10), 20 (S20), 50 (S50), and 70 (S70) km away from the FAIM transect, respectively.

The correlation between changes in geoid/topography ratios and spreading rate exists within ~100 km south of the FAIM transect. Thus, at least in this range, one may expect that an upper mantle density structure similar to that inferred beneath FAIM Line 1 would also predict the geoid/topography ratios along these southern tracks. If this is the case, it may suggest that a similar mechanism (varying crustal/upper mantle structures due to melt-retention) tied to the slow/ultra-slow spreading transition is responsible for the observed correlation. In Figure 4.7, we show the predicted geoid/topography ratios for tracks 10, 20, 50, and 70 km south of the FAIM transect calculated using the predicted geoid of the "*30 km model"* (green lines) from the FAIM transect and the bathymetry from along the southern tracks. Although the fit is not perfect and deteriorates with distance from Line 1, probably because of spatial variability of crust and upper mantle structures, these plot show a decent agreement between observations and predictions.

The method we use to analyze geoid/topography ratios differs from that employed in previous studies [e.g., *Sandwell and Mckenzie,* 1989; *Mark and Sandwell,* 1991], in that we use "instantaneous ratios" calculated by division of geoid height by topography at each location, whereas more typically regional ratios are determined as slopes from least-square fits of geoid versus topography along the tracks. These quantities (Figure 4.4 and 4.4), however, also show flat profiles along the direction of paleo-spreading, consistent with the expected linear relationship between geoid/topography ratios and offset expected in old lithosphere [*Haxby and Turcotte,* 1978]. We can explore this type of analysis by considering the two distinguishable intermediate wavelength (λ ~ 300 - 400 km) components observed in the FAIM transect geoid/topography ratios with a transition

marked by a "ramp" in the offset range km 350 - 400, coinciding with the smooth/rough basement boundary (Figure 4.3). The almost flat profiles of geoid/topography ratios suggest that the linear relationship

$$N(k)/h(k) = 2\pi G\Delta\rho/g\ (1-\exp(kd_c))/k \qquad (4.4)$$

presented by *Haxby and Turcotte* [1978] and *Parson and Daly* [1983] applies. This formula describes the variation of geoid height N/topography h for a wave number k, with compensation by mass deficit $\Delta\rho$ concentrated at a single depth d_c. In the long-wavelength limit, $kd_c<<1$, the wave number dependence drops out and the relationship becomes:

$$N/h = (2\pi G\Delta\rho/g)\ d_c\ . \qquad (4.5)$$

From this equation, based on observed geoid/topography ratios, one can relate a density anomaly $\Delta\rho$ to a given compensation depth d_c, or vice versa. For a fixed d_c, lateral variation in geoid/topography ratio suggests a lateral variation in density structure. Figure 4.5 shows that geoid/topography changes by ~0.2 m/km across the ramp. For a fixed compensation depth, this corresponds to a change in mantle density of ~0.2 kg/m^3 change in mantle density, with less dense mantle in the east. Lateral density variation of this order is in agreement with the average lateral density variations in density models described in Chapter 2 and used in this chapter to model the geoid.

4.5 Discussion

Results from the FAIM transect suggest that the regional rough/smooth basement boundary [*Sundvic et al,* 1984; *Vogt,* 1991], at least below Line 1 (Figure 1.1), is not only a topographic divide, but also marks different crustal/mantle structures. In Chapter 2, we

showed that melt retention provides a plausible explanation for a variety of observational constraints along Line 1. This mechanism predicts that the lateral variation in mantle structure seen along FAIM Line 1 should also exist beneath other crossings of the rough/smooth boundary. To test this notion, we have analyzed geoid/topography ratios, as these ratios ought to be more sensitive to different mass anomalies in the shallow mantle than gravity [*Haxby and Turcotte,* 1978]. The results of our analysis suggest that regional geoid/topography ratios, viewed with the aim of explaining observed structure along the FAIM transect, are more consistent with a melt retention mechanism than a mechanism due to an influence from Bermuda. However, a simple usual correlation of unfiltered geoid/topography ratio with spreading rate change exists only in an area very local to the FAIM transect. The loss of this correlation to the north is not surprising, and may be attributed to lithospheric structure imparted by processes related to Bermuda. The loss of correlation to the south, however, requires further consideration.

Within ~100 km south of the FAIM transect, the fit of detrended predicted geoid/topography ratios gradually deteriorates (Figure 4.7) with distance from Line 1. This deterioration in fit probably represents variability in crustal and upper mantle structure with respect to the FAIM transect. The loss of clear correlation between spreading rate and geoid/topography ratios beyond ~100 km south may indicate that there is not coherent lithospheric signal associate with regional spreading rate change, or it may be due to a non-isostatic component in the geoid.

The interior of the earth is dynamic. Lateral temperature variations give rise to density anomalies that rise and fall in the mantle. Plate tectonics is one expression of these dynamics. Density anomalies in the mantle that are not in equilibrium impart a

long-wavelength dynamic component to the geoid. There are prominent long wavelength undulations in the geoid of the western Atlantic (Figure 4.2), including a NE-SW directed high that extends down from the northern Atlantic, a NE-SW directed low to the east of the high, and a NW-SE directed low that runs just north of the Bahamas. These long-wavelength geoid components are likely due to deep, uncompensated density anomalies. *Vogt* [1991] argues that mantle convection is responsible for the long-wavelength geoid patterns in the western Atlantic. He suggests that the long wavelength geoid low near the continent-ocean boundary may represent downwelling concentrated along the subsiding, sediment-loaded margin, and that the Bermuda swell and the geoid low southeast of the swell (referred to as the Anti-Bermuda swell by *Vogt* [1991]) may be a paired of upwelling/downwelling formed when the Atlantic widened beyond 2000 km. It is possible that the dynamic components of the geoid obscure the generally subtle signal associated with the spreading-rate change at the rough/smooth boundary. This is suggested by the strong, long-wavelength distortion of the observed geoid/topography ratios that intensifies southward on transects that cross progressively more of the eastern geoid low. The analyses described in this chapter all relate to isostatic density structure and so cannot unravel the dynamic signal from the static signal.

4.6 Conclusions

We observe a transition in geoid/topography ratios along the FAIM transect and tracks up to ~100 km south that can be explained by lateral upper-mantle density anomalies. The results obtained from modeling geoid/topography ratios, together with other observations from the FAIM experiment, suggest that the low-density mantle may

be attributable to melt retention during ultraslow spreading. Forward modeling of the geoid signal places constraints on the depth extent of the anomalous mantle that gravity modeling can not, and suggests that the density anomaly is confined to the upper 30-60 km of the mantle. The value of this type of analysis is tempered by an inability to deal with long-wavelength, dynamic geoid components in a straightforward manner. However, the availability of global geoid and bathymetry grids enables this type of analysis to be performed anywhere in the ocean. Further study of the relationship between spreading rate and melt retention could be carried out, for example, at other identified rough/smooth transitions in the Atlantic where dynamic geoid components are less dominant.

CHAPTER 5

CONCLUSIONS

Wide-angle reflection and refraction data, marine gravity anomalies, and geoid versus topography ratios all indicate an abrupt change in crustal and upper mantle properties that correlates with an abrupt roughening of basement morphology as spreading rate slowed. Retention of melt, rather than a reduction in melt production, during slower spreading provides the most satisfactory explanation to all of these observable constraints. This interpretation favors plate-driven mantle flow when this lithosphere formed. The wide melting zone of such a passive system may render off-axis melts susceptible to freezing into the lithosphere or scavenging by fractures before they can be extracted to form crust. The resulting thinner crust of slower-spreading systems is thus comprised preferentially of melts that formed near to the ridge axis. Therefore, this thinner crust may have higher concentrations of incompatible elements, consistent with previous geochemical observations that thin crust formed at spreading rate less than 20 mm/yr are enriched in incompatible elements.

In Chapter 2, we arrive at conclusions based on results of wide-angle seismic data and marine gravity modeling with the tacit assumption that the crust below Line 1 is primarily made up of igneous crust so that the variation in crustal thickness is directly related to either the total melt production or the amount of extracted melt. We test this assumption by analyzing and modeling P-S-P type mode-converted arrivals registered on the vertical component OBSs in Chapter 3. Modeling various multiply reflected mode-converted S-waves reveals a uniform Poisson's ratio of ~0.27 in the lower crust below both Line 1

and Line 2, indicating a dominantly melt-derived gabbroic lithology and thus supporting our igneous-crust hypothesis. Although limited by low signal/noise ratios, especially on the instruments along Line 1, travel-time fits of S_n phases and their multiply-reflected variants below the both lines may suggest mantle Poisson's ratio of ~0.27 and weak (~3 %) SV anisotropy. This result supports *Gaherty et al.'s* [2004] inferences on patterns of ductile deformation during relatively slow spreading based solely on P-wave anisotropy.

In Chapter 4, we show that a transition in geoid versus topography ratios exists along the FAIM transect and parallel tracks within the range of ~100 km south from FAIM, and that this transition correlates with changes in spreading rate. Along FAIM Line 1, geoid/topography ratios are well predicted directly from the density models developed in Chapter 2. In fact, the geoid/topography ratios help to distinguish between these models and suggest that the model with the shallowest anomalous mass distribution (with mass distributed between 30 ~ 60 km depth) is preferred. The presence of low-density lithospheric mantle can be explained by spreading rate dependent melt retention or efficiency of melt extraction. As we show in Chapter 2, this interpretation is compatible with seismic data and marine gravity acquired along the main FAIM transect (Line 1).

The overall results of this study suggest that, at least in some cases, compositional anomalies in the mantle may be emplaced at normal mid-ocean ridges (i.e. away from hotspots) and exist beneath topographically normal seafloor (i.e. not a plateau or swell), persisting over time. These shallow lithospheric structures created by changes in spreading rate bear witness to what happened at mid-ocean ridges in the past and various geophysical methods can detect them.

REFERENCES

Aharonov, E., J. A. Whitehead, P. B. Kelemen, and M. Spiegelman, Channeling instability of upwelling melt in the mantle, *J. Geophys. Res., 100,* 20,433-20,450, 1995.

Au, D., and Clowes, R.M., Shear-wave velocity structure of the oceanic lithosphere from ocean bottom sesmometer studies, *Geophys.J.R.astr.Soc.,* 77, 105-123, 1984.

Birch, F., The velocity of compressional waves in rocks to 10 kilobars, 1, *J.Geophys.Res.,* 65, 1083-1102, 1960.

Birch, F., The velocity of compressional waves in rocks to 10 kilobars, 2, *J.Geophys.Res.,* 66, 2199-2224, 1961.

Boudier, F., and R. G. Colemen, Cross section through the peridotite in the Somali ophiolite, southeastern Oman mountains, *J. Geophys. Res.,* 86, 2573-2592, 1981.

Bown, J. W., and R. S. White, Variation with spreading rate of oceanic crustal thickness and geochemistry, *Earth Planet. Sci. Lett. 121*, 435-449, 1994.

Bratt, S. R., and Purdy, G. M, Structure and variability of oceanic crust on the flanks of the East Pacific Rise between 11° and 13° N, *J. Geophys. Res.,* 89, 6111-6125, 1984.

Braun, M. G., and P. B. Kelemen, Dunite distribution in the Oman ophiolite: Implication for melt flux through porous dunite conduits, *Geochem, Geophys, Geosyst.,* 3, 8603 doi:10.1029/2001GC000289, 2002.

Broucher, T. M., Empirical relations between elastic wavespeeds and density in the earth's crust, *Bull. Seism. Soc. Am.,* 95, 2081-2092, 2005.

Cannat, M., Emplacement of mantle rocks in the seafloor at Mid-ocean ridges, *J. Geophys. Res., 98,* 4163-4172, 1993.

Cannat, M., How thick is the magmatic crust at slow spreading oceanic ridge? *J. Geophys. Res., 101*, 2847-2857, 1996.

Calson, R. L., Gangi, A. F., and Snow, K. R., Empirical reflection traveltime versus depth and velocity versus depth functions for the deep-sea sediment column, *J. Geophys. Res, 91,* 8249-8266, 1986.

Cheung, H.P.Y, and Clowes, R.M, Crustal structure from P-and S-wave analyses:ocean bottom seismometer results in the north-east Pacific, *Geophys.J.R.astr.Soc,* 65, 47-73, 1981.

Christensen, N. I., Elasticity of ultrabasic rocks, *J. Geophys. Res.,* 71, 5921-5931, 1966.

Christensen, N.I, Poisson's ratio and crustal seismology, *J.Geophys.Res,* 101, 3139-3156, 1996.

Christeson, G.L., Shaw, P.R. and Garmany, J.D., Shear and compressional wave structure of the east Pacific rise, 9°-10°N, *J.Geophys.Res,* 10, 1997.

Collier, J.S, and Singh, S.C., Poisson's ratio structure of young oceanic crust, *J.Geophys, Res,* 103, 20,981-20,996, 1998.

Conrad, C. P., Island, the Farallon slab, and dynamic topography of the North Atlantic, *Geology,* 37, 177-180.

Cordery, J. M., and Morgan, J. P., Convection and melting at Mid-ocean ridge, *J. Geophys. Res., 98,* 19,477-19,503, 1993.

Detric, R. S., and Crough, S. T., Island subsidence, hot spots, and lithospheric thinning, *J. Geophys. Res.,* 83, 1236-1244, 1978.

Dick, H. J. B., Abyssal peridotites, very-slow spreading ridges and ocean ridge magmatism, in magmatism in the Ocean Basin, edited by A. D. Saunders and M. J. Norry, *Geol. Soc. Spec. Publ. Londun, 42,* 71-105, 1989.

Dick, H.J.B., J. Lin and H. Schouten, An ultraslow-spreading class of ocean ridge,

Nature, 426, 405-412, 2003.

Ewing, J. I., and Zaunere, R, Seismic profiling with a pneumatic sound source, *J. Geophys, Res,* 69, 4913-4915, 1964.

Fleitout, L, C. Dalloubeix, and C. Moriceau, Small-wavelength geoid and topography anomalies in the south Atlantic ocean: A clue to new hot-spot tracks and lithospheric deformation, *Geophys, Res, Lett.,* 16, 637-640, 1989.

Forsyth, D.W., Geophysical constraints on mantle flow and melt generation beneath mid-ocean ridge, in J.P. Morgan, D.K. Blackman, and J.M. Sinton, Eds., Mantle flow and Melt generation at mid-ocean ridges, *Geophysical Monograph 71, American Geophysical Union,* 1-65, 1993.

Fowler, C.M.R., The solid earth, Cambridge University Press, Cambridge, 1990.

Fryer, G. J. Miller, and P. A. Berge, Seismic anisotropy and age-dependent structure of the upper oceanic crust, in The evolution of mid-ocean ridges, *Geophys, Monogr, Ser.,* 57, edited by J. M. Sintion, 1-8, AGU, Washington, D.C., 1989.

Gaherty, J.B., D. Lizarralde, J. Collins, G. Hirth, and S. Kim, Mantle deformation during slow seafloor spreading constrained by observations of seismic anisotropy in the western Atlantic, *Earth Planet. Sci. Lett.,* 228, 255-265, 2004.

Green, G. F., The lost city 2005 expedition, http://oceanexplorer.noaa.gov/explorations/05lostcity, May/2005.

Grove, T. L., R. J. Kinzler, and W. B. Bryan, Fractionation of mid-ocean ridge basalt (MORB), In Mantle flow and melt generation at mid-ocean ridges, *Geophysical Monograph 71,* 281-310, 1992.

Grow, J.A. and R.G. Markl, IPOD-USGS multichannel sesmic reflection profile from Cape Hatteras to the Mid-Atlantic ridge, *Geology,* 5, 625-630, 1977.

Haxby, W. F. and D. L. Turcotte, On isostatic geoid anomalies, *J. Geophys. Res.,* 83, 5473-5478, 1978.

Hill, M. N, Recent geophysical exploration of the ocean floor, *Phys. Chem. Earth,* 2, 129-163, 1957.

Joket, W., Ritzmann, O., Schmidt-Aursch, M.C., Drachev, S., Gauger, S., and Snow, J., Geophysical evidence for reduced production on the Artic ultraslow Gakkel mid-ocean ridge, *Nature,* 423, 962-965, 2003.

Jha, K., E. M. Parmentier, and J. Phipps. Morgan, The role of mantle-depletion and melt-retention buoyancy in spreading-center segmentation, *Earth Planet. Sci. Lett., 125,* 221-234, 1994.

Jones, E. J. W., Marine Geophysics, Jone Wiely & Sons Ltd, West Sussex, 1999.

Johnston, J.E., and Christensen, N.I, Shear wave reflectivity, anisotropies, Poisson's ratios, and densities of a southern Appalachian Paleozoic sedimentary sequence, *Tectonophysics,* 210, 1-20, 1992.

Kelemen, P. B., Kikawa, E., Miller, D. J., and Leg 210 scientific party, ODP leg 209 drills into mantle peridotite along the Mid-Atlantic ridge from 14°N to 16°N, *JOIDES, J, 30,* 14-19, 2004.

Kelemen, P. B., N. Shmizu, and V. J. M. Salters, Extraction of mid-ocean-ridge basalt from the upwelling mantle by focused flow of melt in dunite channels, *Nature, 375,* 747-753, 1995.

King, S. D., North Atlantic topographic and geoid anomalies: The results of a narrow ocean basin and cratonic root? *In Foulger,* G. R, D. L. Anderson, J. H. Natland, and D. C. Presnall eds., Plate, Plumes&Paradigms, Geol. Soc. Spec, Paper, 388, in press, 2005.

Klitgord, K.D., and H. Schouthen, Plate kinematics of the central Atlantic, in *The Geology of North America,* vol. M, *The western North Atlantic regions,* P.R Vogt and B.E. Tucholke, Eds., *Geol. Soc. Am.,* Boulder, Colo., 19-53, 1986.

Klingelhofer F., Geli, L., Matias, L, Steinsland, L., and Mohr, J., Crustal structure of a super-slow spreading center: a seismic refraction study of Mohns ridge, 72°N, *Geophys. J. Int. 141.,* 509-526, 2000.

Langmuir, C.H., E.M. Klein, and T. Plank, Petrological systimatics of mid-ocean ridge basalts: Constraints on melt generation beneath ocean ridges, in J.P. Morgan, D.K. Blackman, and J.M. Sinton, Eds., Mantle flow and Melt generation at mid-ocean ridges, *Geopphysical Monograph 71, American Geophysical Union*, 183-281, 1993.

Lizarralde, D., and W. S. Holbrook, U.S. mid-Atlantic margin structure and early thermal evolution, *J, Geophys. Res., 102,* 22,855-22,875, 1997.

Lizarralde, D., J.B. Gaherty, J.A. Collins, G. Hirth, and S. Kim, Spreading rate dependence of melt extraction at mid-ocean ridges from mantle refraction data, *Nature, 432*, doi:10.1038/nature03140, 744-747, 2004.

Lonsdale, P, Geomorphology and structural segmentation of the crest of southern (Pacific-Antarctic) East Pacific Rise, *J. Geophys. Res,* 99, 4683-4702, 1994.

Lovecraft, H. P., The White Ship, *In the transition of H.P Lovecraft*, Arkham House Publishers, Inc, New York 1996.

Ludbig, W. J., Nafe, J. E, and Drake, C. L., Seismic refraction, in *The Sea,* A.E. Maxwell eds, 4, Wiely-Interscience, New York, 53-84, 1970.

Malinverno, A. Inverse square-root dependence of mid-ocean ridge flank roughness on spreading rate, *Nature,* 352, 58-60, 1991.

Mark, K. M., and D. T. Sandwell, Analysis of geoid height versus topography for oceanic plateaus and swells using nonbiased linear regression, *J. Geophys. Res.,* 96, 8045-8055, 1991.

MELT experiment team, Imaging the deep seismic structure beneath a mid-ocean ridge, *Science,* 280, 1216-1218, 1998.

Mckenzie, D., and M.J. Bickle, The volume and composition of melt generated by extension of the lithosphere. *J. Petrology, 29,* 625-679, 1988.

Montési, L. G., P. B. Kelemen, and M. Spiegelman, Interaction of dissolution channels with a crystallization front in the shallow mantle beneath mid-ocean ridges, *Eos Trans. AGU, 83*(47), Fall Meet. Suppl., V61A-1344, 2002.

Muller, M.R., C.J., Robinson, T. A., White R.S., and M.J. Bickle, Thin crust beneath ocean drilling program borehole 735B at the southwestIndian Ridge?, *Earth Planet. Sci. Lett., 148*, 93-107, 1997.

Müller, R.D., W. R. Walter, J.-Y. Royer, L. M. Gahagan, & J. G. Scalter, Digital isochrones of the world's ocean floor, *J. Geophys. Res., 102,* 3211-3214, 1997.

Nakamura, Y., P. L. Donoho, P. H. Roper, and P M. McPherson, Large-offset seismic surveying using ocean-bottom seismographs and air guns, Instrumentation and field technique, *Geophysics, 52*, 1601-1611, 1987.

Nicolas, A., Structures of ophiolites and dynamics of oceanic lithosphere, Kuluwer, Dodrecht, 1989.

Ockendon, J. R., and Turcotte, D. L., On the gravitational potential and field anomalies due to thin mass layers, *Geophys, J. R. Astron. Soc.* 48, 479-492, 1978.

Parmentier E.M., and J.Phipps. Morgan, Spreading rate dependence of three-dimensional structure in oceanic spreading centers, *Nature, 348,* 325-328, 1990.

Parson, B., and Daly, S., The relationship between surface topography, gravity anomalies, and temperature structure of convection, *J. Geophys. Res.,* 88, 1129-1144, 1983.

Parsons, B., and D.P. McKenzie, Mantle convection and the thermal structure of the planets. *J. Geophys. Res., 83,* 4485-4496, 1978.

Pickett, G. R., Acoustic character logs and their applications in formation evaluation, *J. Can. Petr. Tech.* 15, 659-667, 1963.

Plank, T., and Langmuir, C. H., Effect of the melting regime on the composition of the oceanic crust. *J. Geophys. Res., 97,* 19.749-19.770, 1992.

Purdy, G.M., The seismic structure of 140 Myr old crust in the western central Atlantic Ocean, *Geophys. J. R. astr. Soc, 72*, 115-137, 1983.

Purdy, G. M., and J. Ewing, Seismic structure of the ocean crust, in *The Geology of North America,* vol. M, *The western North Atlantic regions,* P.R Vogt and B.E. Tucholke, Eds., *Geol. Soc. Am.,* Boulder, Colo., 313-330, 1986.

Raitt, R. W, The crustal rocks *In* M.N.Hill, ed., *The sea*, 3, Interscience, New York, 85-102, 1963.

Reid, I., and H. R., Jackson, Oceanic spreading rate and crustal thickness. *Marine Geophys. Res 5,* 165-172*,* 1981.

Roman, D. R., Wang, Y. M., Henning, W., and Hamilton, J., Assessment of the New National Geoid Height Model, GEOID03 , Proceedings of the American Congress on Surveying and Mapping 2004 meeting., 2004.

Sandwell D. T., and K. R., Mckenzie, Geoid height versus topography for oceanic plateaus and swells, *J. Geophys. Res.,* 94, 7403-7418, 1989.

Sandwell D.T., and Rekin, M, Compensation of swell and plateaus in the north Pacific: No direct evidence for mantal convection, J. Geophys. Res., 93, 2775-2783, 1988.

Shaw, P.R, Age variations of oceanic crust Poisson's ratio: Inversion and a porosity evolution model, *J.Geophys,Res,* 99, 3057-3066, 1994.

Shearer, P. M., Cracked media, Poisson's ratio and the structure of the upper oceanic crust, *Geophys, J.R. Astron. Soc.,* 82,375-414, 1985.

Small C., and D. Sandwell, An abrupt change in ridge axis gravity with spreading rate, 94, J. *Geophys. Res.,* 94, 17,383-17,392, 1989.

Smith W. H., Seafloor tectonic fabric from satellite altimetry, *Annu. Rev. Earth Planet. Sci.* 1998, 26, 697-738, 1998.

Smith W. H. F., and D. T. Sandwell, Global seafloor topography from satellite altimetry and ship depth soundings, *Science,* 277, 1956-1962, 1997.

Smith, D. K., and P. R., Shaw, Seafloor topography: A record of a chaotic dynamical system? *Geophys, Res, Lett,* 17, 1541-1544, 1990.

Sparks, D. W., and E. M. Parmentier, Melt extraction from the mantle beneath spreading centers, *Earth Planet. Sci. Lett., 105,* 368-377, 1991.

Spiegelman, M., P. B. Kelemen, and E. Aharonov, Causes and consequences of flow organization during melt transport: The reaction infiltration instability in compactible media, *J. Geophys. Res, 106,* 2061-2077, 2001.

Spiegelmen, M., and P. B. Kelemen, Extreme chemical variability as a consequence of channelized melt transport, *Geochem. Geophys. Geosyst., 4,* paper number 2002GC000336, 2003.

Spiegelmen, M, and J. R. Reynolds, Combined dynamic and geochemical evidence for convergent melt flow beneath the East Pacific Rise, *Nture, 402,* 282-285, 1999.

Spudich, P, and Orcutt, J, Petrology and porosity of an oceanic crustal site:results from wave form modeling of seismic refraction data, *J. Geophys. Res,* 85, 1409-1433, 1980.

Sotin, C., and E. M. Parmentier, Dynamical consequences of compositional and thermal density stratification beneath spreading centers, *J. Geophys. Res., 16,* 835-838, 1989.

Sundvik, M, R. L. Larson, and R. S. Detrick, Rough-smooth basement boundary in the western north Atlantic basin: Evidence for a seafloor-spreading origin, *Geology.,* 12, 31-34, 1984.

Tolstoy, M., A.J. Harding, and J. A. Orcutt, Crustal thickness on the Mid-Atlantic ridges: bulls-eye gravity anomalies and focused accretion, *Science, 262,* 726-729., 1993.

Turcotte, D.L., and Schubert, G., Geodynamics, Applications of continuum physics to geological problems, John Wiley & Sons, New York, 1982.

Turcotte, D. L, and Morgan J. P, The physics of magma migration and mantle flow beneath a mid-ocean ridge, in J.P. Morgan, D.K. Blackman, and J.M. Sinton, Eds., Mantle flow and Melt generation at mid-ocean ridges, *Geophysical Monograph 71, American Geophysical Union,* 1-65, 1993.

Vogt, P. R, Bermuda and Applachian-Labrador rises: Common non-hotspot prosesses?, *Geology,* 19, 41-44, 1991.

Vogt, P. R., Anderson, C. N., and Bracey, D.R., Mesozoic magnetic anomalies, sea-floor spreading, and geometric reversals in the southwestern North Atlantic: J. Geophys. Res, 76, 4796-4823, 1971.

White, R.S., D. Mckenzie, and R.K. O'nions, Oceanic crustal thickness from seismic measurements and rare earth element inversions, *J. Geophys. Res., 97,* 19,683-19,715, 1992.

White, R. S., T. A. Minshull, M. J. Bickle, and C. J., Robinson, Melt generation at very slow-spreading oceanic ridges: Constraints from geochemical and geophysical data, *J. Petrology., 42,* 1171-1196, 2001.

White, R.S., and R.A, Stephen, Compressional to shear conversion in oceanic crust, *Geophys.J.R.astr.Soc,* 63, 547-565, 1980.

Wyllie, P. J, The way the earth works, Wiely, New York, 1976.

Zandt, G., and Ammon, C. J., Continental crust composition constrained by measurements of crustal Poisson's ratio, *Nature,* 374, 152-154, 1995.

Zelt, C.A., and R.B. Smith, Seismic traveltime inversion for 2-D crustal velocity structure, *Geophys. J.Int., 108,* 16-34, 1992.